https://lib.uliege.be https://matheo.uliege.be

Travail de fin d'études et stage[BR]- Travail de fin d'études : N/A[BR]- Stage d'insertion professionnelle

Auteur : Fassinato, Edoardo
Promoteur(s) : Mertens, Anne; Tchuindjang, Jérôme Tchoufack
Faculté : Faculté des Sciences appliquées
Diplôme : Cours supplémentaires destinés aux étudiants d'échange (Erasmus, ...)
Année académique : 2024-2025
URI/URL : http://hdl.handle.net/2268.2/23955

Avertissement à l'attention des usagers :

Tous les documents placés en accès ouvert sur le site le site MatheO sont protégés par le droit d'auteur. Conformément aux principes énoncés par la "Budapest Open Access Initiative"(BOAI, 2002), l'utilisateur du site peut lire, télécharger, copier, transmettre, imprimer, chercher ou faire un lien vers le texte intégral de ces documents, les disséquer pour les indexer, s'en servir de données pour un logiciel, ou s'en servir à toute autre fin légale (ou prévue par la réglementation relative au droit d'auteur). Toute utilisation du document à des fins commerciales est strictement interdite.

Par ailleurs, l'utilisateur s'engage à respecter les droits moraux de l'auteur, principalement le droit à l'intégrité de l'oeuvre et le droit de paternité et ce dans toute utilisation que l'utilisateur entreprend. Ainsi, à titre d'exemple, lorsqu'il reproduira un document par extrait ou dans son intégralité, l'utilisateur citera de manière complète les sources telles que mentionnées ci-dessus. Toute utilisation non explicitement autorisée ci-avant (telle que par exemple, la modification du document ou son résumé) nécessite l'autorisation préalable et expresse des auteurs ou de leurs ayants droit.

Université de Liège – Università degli Studi di Padova

Faculté des Sciences Appliquées – Dipartimento di Ingegneria Industriale DII

Master’s Thesis in Materials Engineering

Influence of Process Parameters and Build Platform Preheating on Defect Occurrence in L-PBF Inconel 718

Promoters: Prof. Anne Mertens *(Université de Liège)*
Prof. Irene Calliari *(Università di Padova)*

Conducted by: EDOARDO FASSINATO

Academic Year: 2024-2025

ABSTRACT

This study investigates the effect of process parameters — specifically laser power, scanning speed, and build platform preheating — on the quality and defect formation in laser-powder bed fusion Inconel 718 components, with the aim of identifying optimal combinations of parameters for achieving high-quality components. Three different batches of samples were fabricated at different preheating temperatures: 80°C, 300°C, and 500°C. The alloy was investigated in terms of density, using gas pycnometry and optical microscopy, revealing that 300°C preheating yielded the largest number of specimens with optimal quality, whereas 500°C resulted in lower densities and larger defects. Scanning electron microscopy coupled with energy-dispersive x-ray spectroscopy showed the formation of a fine cellular microstructure with oxide inclusions of varying morphologies and compositions, and solidification cracks, in particular in samples printed with the lowest preheating temperature. Finally, a mechanical characterization based on the hardness measurements indicated a general decrease in hardness with increasing preheating temperature.

Contents

ABSTRACT ....

Chapter 1 1

INTRODUCTION 1

Chapter 2 5

STATE OF THE ART 5

  2.1 Additive Manufacturing.. 5

  2.2 Laser-Powder Bed Fusion (L-PBF) 6

    2.2.1 Physics of L-PBF 8

    2.2.2 Setting Parameters 9

    2.2.3 Volumetric Energy Density (VED) 9

    2.2.4 Defects in L-PBF 10

    2.2.5 PV Processing Maps 11

  2.3 Superalloys 12

    2.3.1 Superalloy Classes 13

    2.3.2 Strengthening Mechanisms in Superalloys 15

  2.6 Inconel 718 17

    2.6.1 Microstructure in Wrought Products 17

    2.6.2 Inconel 718 Processed by Laser-Powder Bed Fusion 19

    2.6.3 Thermal Treatments 20

Chapter 3 23

MATERIALS AND EXPERIMENTAL METHODS 23

  3.1 Original Powders 23

  3.2 Sample Fabrication 23

    3.2.1 AconityMIDI Machine 23

    3.2.2 Characteristics and Parameters of the Specimens 25
    3.2.3 Sample Preparation.. 31
  3.3 Microstructural Characterization 32
    3.3.1 Optical Microscope (OM) and ImageJ Analysis 33
    3.3.2 Scanning Electron Microscope (SEM) 33
  3.4 Density Measurements 34
    3.4.1 Density Assessment with Pycnometer 35
    3.4.2 Density Measurement with Micrographs 35
  3.5 Hardness Tests 36
    3.5.1 Macro-Hardness and Micro-Hardness 36
Chapter 4 39
RESULTS 39
  4.1 Density Assessment 39
    4.1.1 Pycnometer Density.. 39
    4.1.2 Density Measurement through Micrographs 42
    4.1.3 Processing Maps 46
  4.2 Internal Defects.. 48
    4.2.1 Porosity Morphologies 48
    4.2.2 Porosity Critical Size 51
    4.2.3 Hot Cracks 52
  4.3 Microstructure 53
    4.3.1 Cellular Structure 53
    4.3.2 Oxide Inclusions 54
  4.4 Mechanical Characterization 56
    4.4.1 Macro and Micro Hardness 56
Chapter 5 59

DISCUSSION ... 59
5.1 Limitations of VED and Effect of Preheating on Process Map and Output Quality ... 59
5.2 Defect and Inclusion Evolution ... 63
5.3 Influence of Process Parameters on Subgrain Boundaries and Size ... 65
5.4 Impact of Parameters and Preheating on Hardness ... 66
Chapter 6 ... 69
CONCLUSIONS ... 69
Chapter 7 ... 71
PERSPECTIVES ... 71
Chapter 8 ... 72
REFERENCES ... 72
Chapter 9 ... 81
ANNEXES ... 81

List of Figures

Figure 1.1 – Schematic representation of work packages (WP) and their interaction in SENSAM+ project, along with the main experimental tasks and models involved, and expected milestones 2

Figure 2.1 – Schematic of laser-powder bed fusion (L-PBF) process [20] 7

Figure 2.2 – Examples of (a) lack-of-fusion defects with unmelted powders [48], (b) keyhole porosities [49], and (c) balling [50] 11

Figure 2.3 – Qualitative representation of PV processing map showing keyhole, balling, and lack of fusion regions [31] 12

Figure 2.4 – Example of face-centered cubic (FCC) unit cell [56] 13

Figure 2.5 – Unit cell of MC (a), M_6C (b), and $M_{23}C_6$ (c) carbides [73] 16

Figure 2.6 – TEM micrographs showing γ' [81] (a) and γ'' [82] (b) particles 18

Figure 2.7 – TEM micrographs showing MC [84] (a), $M_{23}C_6$ [85] (b), and M_6C [86] (c) carbides 19

Figure 2.8 – Micrographs showing the morphology of Laves [88] (a) and δ [89] (b) phases 19

Figure 3.1 – AconityMIDI machine [93] 24

Figure 3.2 – Printed Samples with platform preheating of 80°C (a), 300°C (b), and 500°C (c) 25

Figure 3.3 – 90°/90° scan strategy [94] 25

Figure 3.4 – Distribution of printing parameters for samples printed with 80°C (a), 500°C (b), and 300°C (c) preheating 30

Figure 3.5 – Illustration showing the cutting line, in red, and the building direction of the cubes 31

Figure 3.6 – Struers Citopress-1 [95] (a) and Struers Tegramin-30 [96] (b) 32

Figure 3.7 – Polished samples after preparation with carbon-based paint and exhibiting hardness indentations 32

Figure 3.8 – Olympus BX60 microscope [97] 33

Figure 3.9 – Tescan Clara Ultra-High Resolution SEM [98] 34

Figure 3.10 – AccuPyc II Serie 1345 Pycnometer [99] 35

Figure 3.11 – Example of thresholding performed with ImageJ® software for the evaluation of the density 36
Figure 3.12 – Innovatest Falcon 500G2 hardness tester [100] 37
Figure 3.13 – Schematic of indentation grid for macro-hardness and micro-hardness .. 37
Figure 4.1 – Variation of sample density as a function of VED for specimens printed with 80°C preheating 43
Figure 4.2 – Variation of sample density as a function of VED for specimens printed with 300°C preheating 44
Figure 4.3 – Variation of sample density as a function of VED for specimens printed with 500°C preheating 45
Figure 4.4 – Variation of the optimal VED range for the different preheating temperatures 46
Figure 4.5 – Process map for 80°C (a), 300°C (b), and 500°C (c) platform preheating 47
Figure 4.6 – Gas porosity morphology observed with an optical microscope at 2.5x magnification (a) and with SEM at 300x magnification (b) 49
Figure 4.7 – SEM micrograph showing the selected EDX line for the analysis of some features observed close to a porosity (a) and the corresponding mass percentage profile of the elements along the line (b) 49
Figure 4.8 – Lack-of-fusion porosity morphology at 2.5x magnification (a), with unmelted particles highlighted in red (b) 50
Figure 4.9 – Spatter particle, highlighted in red, on the surface of a sample, with the corresponding underlying defects indicated in green 51
Figure 4.10 – SEM micrograph, with 300x magnification, showing a hot crack (a) and atomic percentage profile of the elements along an EDX line passing through the crack (b) 53
Figure 4.11 – Micrograph showing the cellular structure of L-PBF Inconel 718 54
Figure 4.12 – SEM micrograph of the analyzed region (a) and EDX mapping of the elements (b) 54
Figure 4.13 – SEM micrographs showing irregular (a) and sharp-edged inclusions, indicated with the red arrow (b) 55

Figure 4.14 – SEM micrograph showing the selected EDX line for the analysis of an irregular inclusion (a) and the corresponding atomic percentage profile of the elements along the line (b), with the red box highlighting Si and O peaks 55

Figure 4.15 – SEM micrograph showing the selected EDX line for the analysis of a sharp-edged inclusion (a) and the corresponding atomic percentage profile of the elements along the line (b), with the red box highlighting Al, O, and Ti peaks 56

Figure 4.16 – Macroscopic hardness results of the analyzed samples 57

Figure 4.17 – Microscopic hardness results of the analyzed samples 57

Figure 5.1 – Process maps for 80°C (a), 300°C (b), and 500°C (c) preheating temperatures. Samples highlighted in green boxes combine high measured density (>99.5 %) with defects not exceeding the critical size, whereas samples in orange boxes also exhibit high measured density but contain large defects..62

Figure 5.2 – SEM micrograph showing the coalescence of SiO_2 inclusions in a sample fabricated with 500°C platform preheating (a) and the corresponding atomic percentage profile of the elements along the EDX line (b), with the red box highlighting Si and O peaks 65

List of Tables

Table 3.1 – Chemical composition of Inconel 718 powders 23

Table 3.2 – AconityMIDI technical sheet [93] 24

Table 3.3 – List of process parameters used for the samples fabrication with 80°C preheating, with the samples highlighted in red that are those not fully printed........... 27

Table 3.4 – List of process parameters used for the samples fabrication with 500°C preheating, with the samples highlighted in red that are those not fully printed........... 28

Table 3.5 – List of process parameters used for the samples fabrication with 300°C preheating, with the samples highlighted in red that are those not fully printed........... 29

Table 4.1 – Pycnometer density for the samples printed with 80°C preheating.............40

Table 4.2 – Pycnometer density for the samples printed with 300°C preheating........... 41

Table 4.3 – Pycnometer density for the samples printed with 500°C preheating........... 42

Table 4.4 – Density measured from micrographs for samples printed with 80°C preheating. Values highlighted in green correspond to samples with a density higher than 99.7%. 43

Table 4.5 – Density measured from micrographs for samples printed with 300°C preheating. Values highlighted in green correspond to samples with a density higher than 99.7%. 44

Table 4.6 – Density measured from micrographs for samples printed with 500°C preheating. Values highlighted in green correspond to samples with a density higher than 99.7%. 45

Table 4.7 – List of the samples selected for further analyses 48

Table 4.8 – Equivalent diameter of the largest porosity in each printed sample for the three different preheating temperatures 52

Table 4.9 – Macro hardness and micro hardness average values for each sample......... 58

Chapter 1

INTRODUCTION

This Master's Thesis is part of a broader research project entitled Smart enhancement of Ni-based superalloys "for additive manufacturing" towards improved creep resistance at high temperature (SENSAM+), which aims at modifying the well-known alloy Inconel 718 to reach both a good printability by Laser-Powder Bed Fusion (L-PBF) and superior creep properties (in as-built and/or heat-treated conditions). To this goal, SEMSAM+ relies on a rigorous methodology and on a well-balanced scientific consortium built on 3 multidisciplinary and complementary teams to combine experimental and modelling approaches.

A major challenge remains to produce defect-free Additive Manufactured (AM) parts, with usage properties equivalent to or higher than those obtained from conventional processes.

The proposed methodology combines experimental and numerical approaches with defined work packages (WP) that interact with one another, as illustrated in Figure 1.1. More specifically, WP1 (Manufacturing & Characterization) will allow printing and characterizing new alloy compositions under both as-built and heat-treated conditions. WP2 (Process Modeling) will help understand the influence of the L-PBF processing parameters on the melt pool (MP) based on P-FEM models. Simultaneously, WP3 (Final Behavior Modeling) will link the microstructures and the usage properties, i.e., in particular, the creep behavior of the printed materials.

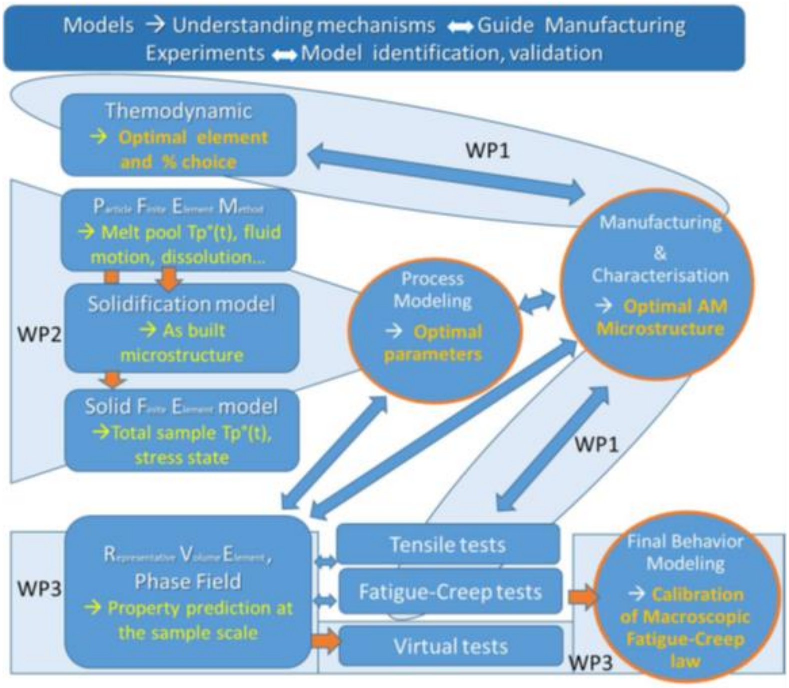
Models → Understanding mechanisms ⟷ Guide Manufacturing
Experiments ⟷ Model identification, validation
Themodynamic
→ Optimal element and % choice
WP1
Particle Finite Element Method
→ Melt pool Tp°(t), fluid motion, dissolution...
Solidification model
→ As built microstructure
WP2
Solid Finite Element model
→Total sample Tp°(t), stress state
Process Modeling
→ Optimal parameters
Manufacturing & Characterisation
→ Optimal AM Microstructure
WP1
Representative Volume Element, Phase Field
→ Property prediction at the sample scale
WP3
Tensile tests
Fatigue-Creep tests
Virtual tests
WP3
Final Behavior Modeling
→ Calibration of Macroscopic Fatigue-Creep law

Figure 1.1 – Schematic representation of work packages (WP) and their interaction in SENSAM+ project, along with the main experimental tasks and models involved, and expected milestones

The work carried out during this master's thesis is part of WP1, which consists of investigating the effect of key process parameters, such as laser power, scanning speed, and platform preheating, on the processability of Inconel 718 powders and on the defect occurrence in the as-built specimens. Therefore, the focus will be on the characterization of the alloy in order to identify the most effective combinations of these processing parameters, which will subsequently be used in further research on creep behavior.

The content of this manuscript is structured as follows:

- Chapter 1 provides an introduction and background to the research.
- Chapter 2:
    - set the state of the art in AM technologies in general and the L-PBF process in particular;
    - highlights the main processing parameters for L-PBF, the type of characterization via defects, and approaches for printing optimization using processing maps;
    - introduces superalloys with their strengthening mechanism;

    - focuses on Inconel 718 while comparing the conventional wrought grade with the newly developed AM grade, and related subsequent heat treatments.
- Chapter 3 presents both the powder feedstock and the experimental methods that have been used, starting from sample preparation up to macro and microstructural characterization.
- Chapter 4 gives the main observations and results related to specimens' soundness, microstructure characterization, and hardness.
- Chapter 5 sets a discussion about the results while addressing relevant issues.
- Chapter 6 corresponds to the main conclusions.
- Chapter 7 draws out some prospects.
- Annexes are also provided at the end of the manuscript.

Chapter 2

STATE OF THE ART

2.1 Additive Manufacturing

Over the past few decades, Additive Manufacturing (AM) has emerged as a highly significant technology for the production of metallic components, exhibiting a great number of advantages over conventional manufacturing methods. Traditional processes are often constrained in terms of achievable geometries and design flexibility [1], [2]. In contrast, AM is a technique that allows the fabrication of complex, near-net-shape components directly from CAD models using a layer-by-layer approach. This eliminates the need for extensive post-processing operations and overcomes many design limitations [3]. Beyond its design flexibility, AM can produce microstructures different from those obtained through conventional techniques, thanks to the unique thermal conditions of the process, potentially enhancing mechanical performance and ensuring greater chemical uniformity [4], [5]. These combined advantages make additive manufacturing extremely attractive, particularly in the aerospace, biomedical, and automotive sectors among all [6], [7].

The birth of additive manufacturing technologies can be traced back to the issuing of the stereolithography patent by the company '3D Systems' [8]. Initially, additive manufacturing was being employed for rapid prototyping, which was developed more than thirty years ago for producing non-structural components for design purposes [6]. However, significant improvements have been made over the past years, thanks to the development of novel additive manufacturing processes and the introduction of new materials with improved mechanical, thermal, and chemical properties [1], [9]. In the particular case of metals, technological advancements led to an increase in part density and overall component quality [10].

Despite the huge improvements, additive manufacturing still faces several limitations in terms of processable materials [9]. In powder-based AM technologies, surface roughness and the so-called 'staircase effect' — particularly evident on inclined surfaces — remain major obstacles to part accuracy [11]. Furthermore, repeatability and reproducibility continue to hinder a high outcome quality, as process parameter fluctuations can affect the final properties of the product [12]. So far, technologies involving the fusion of powders have yet to deliver component quality equivalent to that of traditional subtractive techniques [8].

According to ISO/ASTM 52900 standard [13], it is possible to distinguish among 7 distinct AM categories:

- Vat Photopolymerization (VPP), which uses a vat of liquid photopolymer resin cured through light-activated polymerization.
- Material Extrusion (MEX), in which material is selectively dispensed through a nozzle.
- Material Jetting (MJT), in which droplets of material are selectively deposited.
- Binder Jetting (BJT), which uses a liquid bonding agent to selectively join powder particles.
- Powder Bed Fusion (PBF), in which thermal energy fuses the desired regions of a powder bed. The energy source can be either a laser or an electron beam.
- Directed Energy Deposition (DED), in which thermal energy is used to fuse materials as they are being deposited.
- Sheet Lamination (SHL), which uses sheets of material bonded together to form an object.

2.2 Laser-Powder Bed Fusion (L-PBF)

Metal powder bed fusion (PBF) is a category of additive manufacturing that involves the interaction of fed powders with a high-energy thermal source. Depending on the specific technique, this energy source can be a laser, as in laser-powder bed fusion (L-PBF), or an electron beam, as in electron beam-powder bed fusion (EB-PBF) [14]. Powder bed fusion is one of the most popular additive manufacturing technologies used for metal part fabrication, offering the possibility to produce components with complex shapes and mechanical properties comparable to those fabricated through conventional manufacturing techniques [15].

The process begins with the preparation of computer-aided design (CAD) files, which are subsequently sliced into two-dimensional layers by computer software. The powders are spread uniformly on the working platform utilizing a recoater, and then the energy source selectively melts regions of the powder bed according to the shape defined by the digital model. Once a layer is completed, the platform lowers by a predetermined layer thickness, and the sequence is repeated until the final component is fully fabricated [16], [17], [18], [19]. **Error! Reference source not found.** provides a schematic representation of the laser-powder bed fusion process.

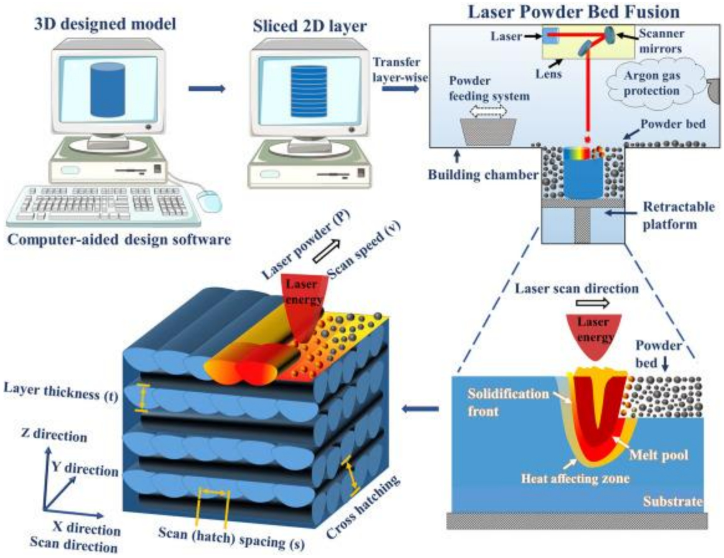
3D designed model
Sliced 2D layer
Laser Powder Bed Fusion
Laser
Scanner mirrors
Lens
Transfer layer-wise
Powder feeding system
Argon gas protection
Powder bed
Building chamber
Retractable platform
Computer-aided design software
Laser powder (P)
Scan speed (v)
Laser energy
Laser scan direction
Laser energy
Powder bed
Solidification front
Melt pool
Heat affecting zone
Substrate
Layer thickness (t)
Z direction
Y direction
X direction
Scan direction
Scan (hatch) spacing (s)
Cross hatching

Figure 2.1 – Schematic of laser-powder bed fusion (L-PBF) process [20]

In certain cases, laser-powder bed fusion can involve the preheating of the working platform to minimize the rapid cooling rate from the base. This approach helps reduce thermal stresses, thus minimizing the risk of deformation and cracks, particularly at the contact point between the sample and the platform [21], [22]. In addition, the build platform is located in a chamber maintained under a controlled atmosphere with a homogeneous flow of inert gas, typically argon or nitrogen, to prevent melt pool oxidation and to facilitate the removal of by-products generated during the powder processing [23].

2.2.1 Physics of L-PBF

The first stage of the fabrication process, in L-PBF, involves the interaction between the incident laser beam and the powder bed. This interaction governs the fraction of energy that is absorbed by the powders, which in turn controls the stability of the melt pool and ultimately the quality of the built component [24]. The absorption, moreover, is controlled by several factors, including the properties of the laser used, the optical properties of the alloy, and the morphology and size distribution of the powders [25], [26]. Fine particles generally exhibit greater energy absorption due to their larger ratio between surface area and volume; however, excessively fine powders can compromise the flowability [27]. Other factors influencing laser absorption include the presence of surface oxides, which can significantly modify the absorptivity of the powders, and the packing density, which governs the laser penetration within the layer [28], [29].

The properties of the particles and the processing parameters used cooperate in the determination of the geometry and stability of the melt pool, which in turn dictate the final quality of the part. The flow of the metal within the melt pool is controlled by Marangoni convection, which induces outward flow from the hot center toward the tail. This effect widens the pool and promotes fusion uniformity [30]. Another important phenomenon is recoil pressure, generated by the vaporization of metal. This pressure may increase the instability of the melt pool, leading to the possibility of gas entrapment [31]. Thus, a careful optimization of the parameters is essential to control the melt pool behavior and achieve defect-free components.

In L-PBF, once the laser passes, the melt pool undergoes rapid solidification with cooling rates typically ranging from 10^5 to 10^8 K/s, far higher than those observed in conventional casting. Normally, such extreme cooling rates produce a fine microstructure that can enhance mechanical properties [32], [33]. Furthermore, heat is predominantly extracted in the build direction, leading to the formation of columnar grains aligned with the thermal gradient. During solidification, both segregation phenomena and the formation of secondary phases can occur. Under the high cooling rates characteristic of L-PBF, coarse precipitates and non-equilibrium phases can form [34].

In L-PBF, the steep thermal gradients and rapid thermal cycling generate strong thermal stresses within the fabricated components. As the molten metal cools down, the track solidifies and contracts; however, the constraints imposed by the underlying solidified layer prevent free deformation, resulting in the generation of residual stresses [14], [31]. When sufficiently high, these stresses can potentially manifest as distortion or warping of the printed component [7]. The magnitude and distribution of residual stresses are highly sensitive to scan strategy and build-plate preheating, which can induce thermal gradients in the material if not optimized [10], [19].

2.2.2 Setting Parameters

In modern laser-powder bed fusion systems, over one hundred processing parameters influence the fabrication process. Among these, the most commonly considered include:

- laser-related parameters, including laser power and spot size;
- scan-related ones such as scan velocity, hatch spacing, and scan strategy;
- powder-related parameters, encompassing particle size distribution and morphology, and layer thickness;
- build chamber and platform parameters such as preheating temperature and atmosphere [35].

The final quality of the product is strongly influenced by these input parameters and their control during the process, as they contribute to the formation of defects, thus altering the mechanical and microstructural properties of the fabricated component [36]. These parameters, most of the time, interact non-linearly, thus requiring a trade-off for achieving the optimization of the process [37]. In order to minimize the occurrence of defects, precise monitoring and control of the process must be implemented to ensure the stability of the build conditions [38], [39].

2.2.3 Volumetric Energy Density (VED)

As described above, input parameters in laser-powder bed fusion (L-PBF) directly affect the quality of the fabricated component. One way to describe the combined effect of the multiple parameters involved is through the energy density indices, which group specific variables into a single value and help in predicting the final properties of the part [31], [40].

Different kinds of energy density have been introduced for this purpose; each of them takes into consideration different parameters [21], [31], [41]:

- Linear energy density (LED) [J/mm]

$$LED = \frac{P}{SS} \tag{1}$$

- Areal energy density (AED) [J/mm^2]

$$AED = \frac{P}{SS \cdot HD} \tag{2}$$

- Volumetric energy density (VED) [J/mm^3]

$$VED = \frac{P \cdot \eta_p}{SS \cdot HD \cdot LT} \tag{3}$$

where P represents the laser power (W), η_p is powder absorptivity (adimensional), SS is scan speed (mm/s), HD refers to hatching distance (mm), and LT is the layer thickness (mm). In certain cases, it is possible to substitute, in the VED formulation, the hatching distance with the laser beam diameter (mm) and the layer thickness with the melt pool depth (mm) [21], [31]. Among these, volumetric energy density is the most widely adopted, as it provides the possibility to qualitatively foresee the properties of the output [31]. However, some studies have highlighted that different parameter combinations yielding the same VED can result in changes in part density [42].

From the perspective of component density, a general trend has been observed: as VED increases from low values, material density improves progressively. However, beyond a certain value, further increases in volumetric energy density result in a gradual decrease in density [43]. At low energy densities, insufficient energy input results in incomplete melting and the formation of lack-of-fusion porosities. Conversely, high energy densities can induce the development of keyhole porosities due to the possible evaporation of the powders, combined with turbulence of the melt pool [41], [43].

The divergencies in output quality when considering the same VED can be correlated to the limitations of (*3*), which takes into account just a limited number of parameters, not considering the actual physics of the melt pool and other processing parameters such as scanning patterns and the direction of gas flow [39], [44].

2.2.4 Defects in L-PBF

Lack-of-fusion defects (Figure 2.2a) typically arise when the laser power is insufficient to ensure adequate penetration of the melt pool into the underlying layer. These defects are also correlated to high scanning speeds that determine a reduced interaction time between the laser and the powders. Lack-of-fusion pores generally appear elongated and irregular in shape and may contain unmelted powder particles within [6], [45], [46]. Their formation is further promoted when hatch spacing is excessive, a condition that does not permit the correct overlapping between adjacent scan tracks, leaving unbonded regions between melt pools [45]. This kind of porosity is often aligned along layer boundaries and can determine stress concentration, which significantly reduces fatigue resistance and the overall mechanical performance [47].

Keyhole defects (Figure 2.2b) occur at excessive energy inputs — typically at high laser powers combined with low scanning velocities — causing a switch from conduction to keyhole mode for heat transfer. In this regime, the alloy can vaporize, generating high recoil pressure, which induces the formation of a vapor cavity. These cavities are often unstable, and they may collapse, entrapping gas within the solidifying material [31], [46]. The resulting pores are generally spherical and located much below the layer surface, which makes them less detrimental for mechanical properties compared to lack-of-fusion defects [43].

A combination of high power and scanning speed can, instead, promote the formation of melt pools with reduced widths and elongated tails, increasing the likelihood of balling defects (Figure 2.2c). Under these conditions, molten metal tends to fragment into spherical droplets rather than forming a continuous track, as it seeks to minimize its surface energy. Balling is typically also influenced by fluid dynamics and surface tension [31].

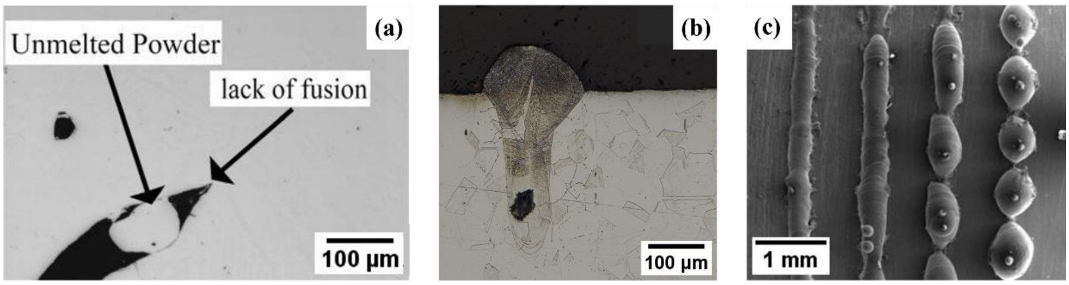

Figure 2.2 – Examples of (a) lack-of-fusion defects with unmelted powders [48], (b) keyhole porosities [49], and (c) balling [50]

2.2.5 PV Processing Maps

Power-velocity (PV) processing maps are extremely helpful in identifying the effects of L-PBF parameters on output quality. These maps permit the identification of the operating window, which encompasses the range of parameters that ensure the production of defect-free components [31]. As illustrated in Figure 2.3, deviations from this optimal parameter range can lead to the formation of different types of porosity defects: lack-of-fusion, keyhole, and balling [45], [46], [51].

PV maps are widely used tools for visualizing the influence of L-PBF parameters on defect formation; however, these maps only consider two parameters — typically laser power and scanning speed — omitting other parameters that can also have a significant impact on the final component quality [31].

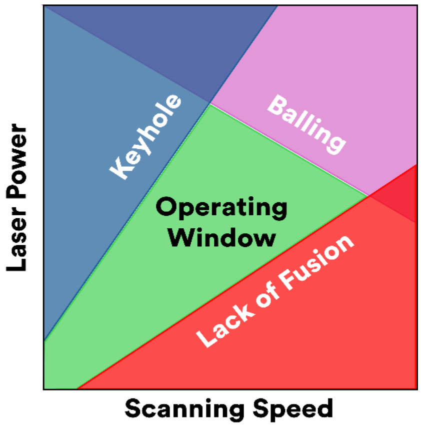

Figure 2.3 – Qualitative representation of PV processing map showing keyhole, balling, and lack of fusion regions [31]

2.3 Superalloys

A superalloy can be considered as an alloy based on elements such as nickel, cobalt, or even iron, if combined with a high percentage of nickel, to which a large number of alloying elements are usually added. The most important feature characterizing these alloys is the combination of both high mechanical properties and high-temperature resistance, making them extremely suitable for fabricating gas turbine engines [52].

The addition of a large number of alloying elements makes superalloys one of the most compositionally complex metallic materials. The proportion of alloying elements is of extreme importance as it influences the overall properties of the alloy [52], [53], [54]. This is made possible by the fact that each element is able to promote the formation of different phases in the alloy [55]. However, this complexity is then reflected in the higher costs associated with this material [52].

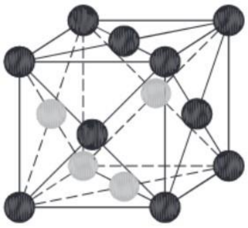

Figure 2.4 – Example of face-centered cubic (FCC) unit cell [56]

Superalloys share a common base microstructure consisting of a face-centered cubic (FCC) matrix (Figure 2.4), within which it is possible to find various dispersed secondary phases, playing a fundamental role in determining the alloy's properties [52], [53], [57]. The FCC matrix is typically responsible for the excellent ductility and toughness, while the precipitates and secondary phases act as primary strengthening agents of the alloy.

Of the three fundamental elements of superalloys — Ni, Co, and Fe — only nickel exhibits an FCC crystal structure at room temperature. In contrast, cobalt and iron adopt other crystal structures at room temperature and transform to FCC only at high temperatures. This means Ni plays a crucial role as an FCC stabilizer throughout the operating temperature range, even when the base element is cobalt or iron [52], [53].

Superalloys are typically classified based on the predominant element that constitutes them. Thus, it is possible to distinguish Fe-based (also Fe-Ni-based), Co-based, and Ni-based superalloys [54].

2.3.1 Superalloy Classes

Iron-nickel alloys are a class of superalloys used for the production of gas turbine engine components such as blades, discs, and casings. They combine high toughness, excellent ductility, and low thermal expansion at elevated temperatures, along with the lower costs associated with the substitution of nickel with less expensive iron. These attributes contribute to their great diffusion, compared with the other superalloy classes [52], [58], [59], [60].

These alloys usually employ two different strengthening mechanisms: solid solution strengthening and precipitation hardening. Moreover, the addition of elements such as aluminum, niobium, and carbon promotes the formation of γ'-Ni_3(Al, Ti), γ"-Ni_3Nb, and some carbides, all of which are important for improving the material properties [58].

The category of cobalt-base superalloys includes those alloys in which the predominant element is cobalt. They are primarily employed in applications where hot corrosion is fundamental or in components operating at moderate-to-high temperatures that are not subjected to high mechanical stresses. Examples include gas turbine vanes and combustor liners [52], [55], [61]. Compared with nickel-base superalloys, they generally exhibit lower strength at intermediate temperatures, but retain their strength to higher temperatures, making them better than nickel ones [62], [63].

The strengthening relies mainly on the formation of carbides in the matrix and in solid solution hardening, while the precipitation mechanism in these alloys is not as effective as the γ' and γ" phases that typically form in nickel-iron- and nickel-base superalloys [52]. Cobalt-base alloys exhibit the precipitation of γ'-Co_3Ti and Co_3Ta, but their instability at high temperatures contributes to the limited adoption of these alloys commercially [62], [64].

Nickel-base superalloys are those in which nickel is the predominant element, enriched by the addition of different alloying elements. Their exceptional relevance stems mainly from their ability to retain their strength even at remarkably high temperatures, while offering great corrosion resistance [52], [65]. These properties make them extremely suitable in aerospace applications and in other demanding environments [52], [66]. When fabricated through powder metallurgy techniques, nickel-base superalloy can achieve a more homogeneous microstructure, not obtainable through casting [22].

The primary strengthening mechanism in nickel-base superalloys is precipitation hardening. Sufficient additions of aluminum and titanium, as alloying elements, promote the formation and precipitation of the γ'-Ni_3(Al, Ti) phase, which is responsible for the higher resistance at elevated temperatures [22], [52]. In the case of niobium-strengthened alloys, such as Inconel 718, the improved mechanical properties come, instead, from the precipitation of γ"-Ni_3Nb phase [59]. While solid solution strengthening can prove to be another effective strengthening mechanism, precipitation hardened alloys remain those exhibiting better overall properties [52].

2.3.2 Strengthening Mechanisms in Superalloys

The strength of the superalloy generally derives from a combination of strengthening mechanisms, including solid solution hardening, precipitation hardening, and dispersion strengthening. While these mechanisms may be present simultaneously, one typically dominates over the others [52].

Solid solution hardening occurs when certain alloying elements are soluble within the matrix of the superalloy and occupy substitutional lattice positions within the FCC matrix [67]. The atomic radius mismatch between the solute atoms and the matrix atoms results in a local distortion of the lattice, generating a consequent strain field that interacts with the dislocations by inhibiting their motion and making plastic deformation much more difficult [67], [68], [69]. This effect assumes great relevance as it contributes to the improvement of the creep strength of the alloy [67].

The effectiveness of solid solution hardening increases with a greater atomic radius mismatch between the matrix elements and the substitutional ones. Larger solute atoms are generally more effective, thanks to their lower diffusion coefficient. However, excessive mismatch can promote the formation of topologically closed-packed (TCP) phases, which can degrade both the strength and the ductility of the alloy. Consequently, a maximum difference between the atomic radii of 10 % is desirable [52], [67].

A certain degree of strengthening in superalloys can also arise from the precipitation of secondary phases — most notably γ' and γ'' — from the FCC matrix. These precipitates act by blocking the movement of the dislocations, thereby enhancing high-temperature strength [52]. The elements normally favoring this strengthening mechanism are titanium and aluminum, which are responsible for the formation of γ' phase, the predominant hardening phase in most nickel-base superalloys. Niobium, or sometimes molybdenum, contributes to the formation of γ'' phase, which is particularly relevant in alloys such as Inconel 718 [52], [70]. The effectiveness of precipitation hardening depends primarily on the volume fraction and the size of the strengthening phases [67].

Strengthening occurs through interaction mechanisms between dislocations and precipitates. The dislocation may shear through a precipitate, causing a certain degree of disorder between the matrix and the precipitate. Alternatively, a precipitate can be bypassed following the Orowan mechanism of dislocations [52], [67].

A related mechanism, called dispersion strengthening, relies on the dispersion of non-coherent oxide particles that are introduced into the alloy rather than precipitated from the matrix. These particles also obstruct the motion of dislocations, contributing to the high-temperature strength [52].

Another important strengthening mechanism in superalloys is carbide hardening, which arises from the precipitation of carbides within the γ matrix. These carbides form through the combination of carbon, which must be present in sufficient percentages, and carbide-forming elements such as molybdenum, niobium, titanium, and chromium [67], [71]. Primary carbides most often assume the formula MC (Figure 2.5 – Unit cell of MC (a), M_6C (b), and $M_{23}C_6$ (c) carbides [73]a); however, during prolonged exposure to elevated temperatures, they tend to transform into M_6C and $M_{23}C_6$ carbides (Figure 2.5b-c), frequently concentrated along grain boundaries [52], [67].

$M_{23}C_6$ carbides are typically enriched in chromium, and their precipitation can deplete the surrounding matrix of chromium, enhancing the susceptibility of the alloy to environmental degradation [52], [72]. Furthermore, the decomposition of primary carbides leads to the release of carbide-forming elements back into the matrix, which, over a certain limit, can cause the formation of deleterious phases to the alloy properties [72].

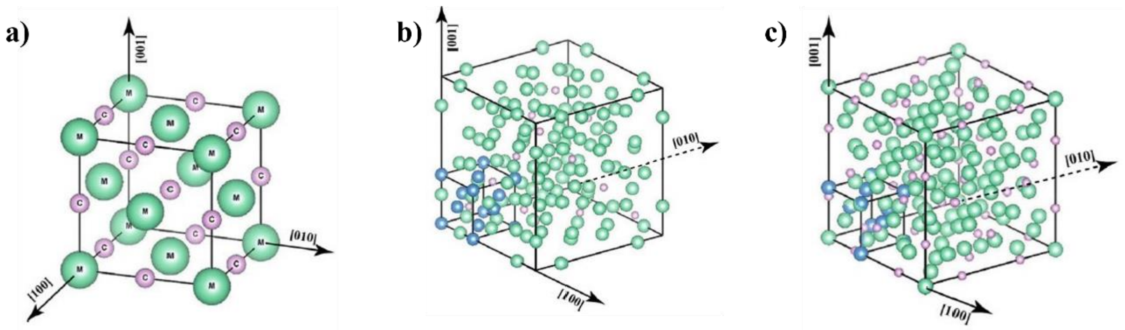

Figure 2.5 – Unit cell of MC (a), M_6C (b), and $M_{23}C_6$ (c) carbides [73]

Despite these potential drawbacks, carbides normally act by improving the creep resistance of the alloy, thanks to their capability of pinning dislocations and grain boundaries, thereby inhibiting grain boundary sliding [52], [74].

2.6 Inconel 718

Inconel 718 is a nickel-chromium-based superalloy belonging to the Ni-Fe family, specifically developed for high-temperature structural applications. It exhibits a combination of high strength, corrosion resistance, and oxidation resistance, all of which are maintained over a wide range of temperatures. This combination of properties makes it suitable for demanding environments where components are subjected to high mechanical stresses and aggressive environments [41], [75], [76].

The exceptional performance of the alloy at elevated temperatures, combined with good weldability and relatively low susceptibility to hot cracking compared to other superalloys, led to its widespread adoption in aerospace applications — such as turbine disks, compressor blades, and casings — as well as in the energy sector for gas turbine components, and in the oil industry [77], [78], [79].

Furthermore, Inconel 718 can be processed using both conventional methods and advanced manufacturing technologies, such as L-PBF. This versatility further increased its importance and adoption for high-performance applications.

2.6.1 Microstructure in Wrought Products

The microstructure of Inconel 718 comprises a matrix (γ phases) and a series of secondary phases, each contributing to defining the mechanical properties and the thermal stability of the alloy.

The γ matrix is the primary phase of Inconel 718, and it is an FCC solid solution containing mainly Ni, Fe, and Cr elements. This matrix provides a good basis for the mechanical performance of the alloy and permits the dissolution of large quantities of alloying elements necessary for the formation of secondary phases [52], [80].

The γ′ phase (Figure 2.6a), typically composed of $Ni_3(Al, Ti)$, has an FCC structure. Despite its volume fractions being smaller compared to other Ni-based superalloys, γ′ still contributes to precipitation hardening of the alloy [52], [80].

The alloy’s primary strengthening phase is γ″ (Figure 2.6b), a body-centred tetragonal (BCT) metastable precipitate with a disc-like morphology and a composition that is Ni_3Nb. Its coherence with the matrix inhibits the sliding of the dislocations, thereby providing high strength to the alloy up to approximately 650°C. Exposure beyond this temperature can trigger its transformation into the δ phases, causing a decrease in strength [41], [52].

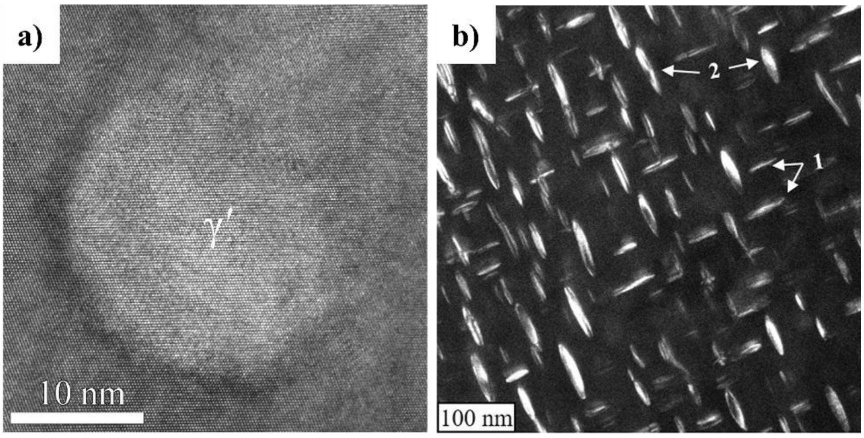

Figure 2.6 – TEM micrographs showing γ' [81] (a) and γ'' [82] (b) particles

The δ phase (Figure 2.8b) shares the same nominal composition of γ″ but has an orthorhombic structure and is incoherent with the γ matrix. As mentioned **Error! Reference source not found.**, it typically precipitates during prolonged exposure to temperatures above 650°C, which can cause a reduction in matrix strength. However, in some cases, δ precipitation can provide a beneficial effect by pinning grain boundaries and controlling grain growth [41], [52], [83].

Carbides in Inconel 718 form as MC (Figure 2.7a), $M_{23}C_6$, (Figure 2.7b), and M_6C (Figure 2.7c), where M can be represented by Nb, Ti, or Mo. Primary carbides of the MC-type form during solidification and remain stable at high temperatures, enhancing creep resistance. With prolonged service, these carbides may decompose into M_6C and $M_{23}C_6$ types [52].

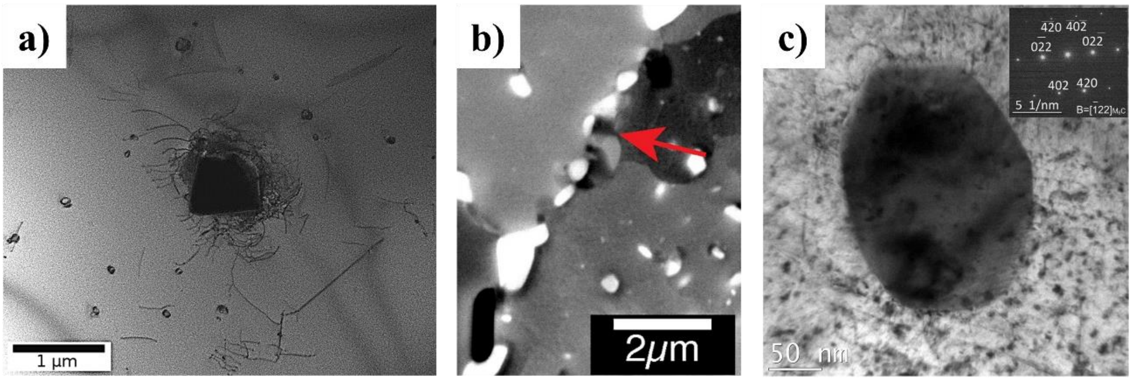

Figure 2.7 – TEM micrographs showing MC [84] (a), $M_{23}C_6$ [85] (b), and M_6C [86] (c) carbides

Finally, the Laves phase (Figure 2.8a) can be found in interdendritic regions of Inconel 718. This phase, however, is considered detrimental because it both reduces the availability of Nb for γ″ precipitation and introduces brittleness into the microstructure. Its presence is strongly affected by cooling rate, Nb content, and processing parameters, and it can be dissolved through post-processing treatments [18], [33], [87].

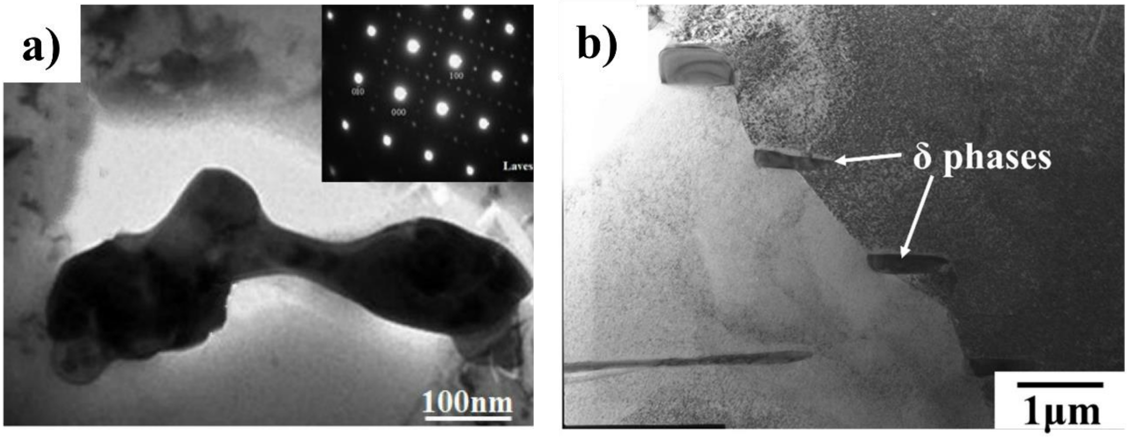

Figure 2.8 – Micrographs showing the morphology of Laves [88] (a) and δ [89] (b) phases

2.6.2 Inconel 718 Processed by Laser-Powder Bed Fusion

The extremely high cooling rates inherent to L-PBF promote the formation of a non-equilibrium microstructure in Inconel 718, which differs from that observed in conventionally cast or wrought alloys. This rapid solidification results in a fine cellular structure preferentially aligned with the build direction due to the thermal gradients [41], [90]. Moreover, a characteristic feature of L-PBF Inconel 718 is the segregation of Nb at interdendritic regions, which often promotes the formation of Laves phases, detrimental for the mechanical properties of the alloy [18], [33].

For ensuring the dissolution of the detrimental Laves phases and for homogenizing Nb distribution, post-processing heat treatments are typically required after the fabrication [91]. Additionally, these treatments promote the precipitation of the strengthening γ' and γ'' phases, which significantly contribute to enhancing the strength, creep resistance, and fatigue life of the component, often bringing the performance closer to that of the wrought counterparts [91].

A further challenge in L-PBF is the accumulation of residual stresses, which can result in cracking, porosity formation, and distortion. Nevertheless, Inconel 718 exhibits a relatively low susceptibility to hot cracking, which makes it particularly suitable for additive manufacturing processes [2]. Another drawback of Inconel 718 fabricated through L-PBF is the development of anisotropy in mechanical properties, which, however, can be mitigated with appropriate thermal treatments or hot isostatic pressing (HIP) [18], [41].

2.6.3 Thermal Treatments

Inconel 718 components, especially when fabricated through the L-PBF technique, are prone to critical issues such as porosity formation, residual stresses, and distortions, all of which can negatively affect the performance [71]. Consequently, thermal treatments during post-processing are crucial for optimizing the properties of the built components [4], [79]. To address these issues and enhance the mechanical properties, various treatments are employed, such as stress relieving, hot isostatic pressing (HIP), homogenization annealing, and aging [91].

Stress relieving aims to alleviate the residual stresses induced by the rapid solidification inherent to L-PBF. These stresses, if not relieved, can compromise the mechanical properties of the alloy. This heat treatment is typically performed at sufficiently high temperatures with extended holding times, which can lead to a partial recrystallization of the microstructure [7], [18].

Hot isostatic pressing (HIP) is widely used to reduce the porosity developed during the fabrication and to close internal cracks that may form, thereby densifying the component [7], [92]. This treatment often promotes recrystallization and grain coarsening, transforming the columnar grains into randomly oriented equiaxed grains [91]. However, while HIP contributes to improving the density of the components, it can also reduce the hardness, a result attributed to the possible grain growth and dissolution of strengthening precipitates such as γ″ [18].

Homogenization annealing, also called solution treatment, is typically performed prior to aging to dissolve undesirable phases such as Laves and δ ones, resulting in a more homogeneous and stress-relieved microstructure [41]. This process promotes grain coarsening and partial recrystallization [2]. Although solution treatment may initially lower the strength, it typically improves the ductility of the alloy through the coarsening of the subgrains [91].

Finally, aging is a heat treatment that can be performed in either a single or double step, and it is fundamental for controlled precipitation of secondary phases, in particular γ′ and γ″, which are the principal strengthening phases in Inconel 718. These strengthening nanoprecipitates formed during this process significantly enhance both room-temperature and high-temperature strength and hardness of the alloy [7], [41].

Chapter 3

MATERIALS AND EXPERIMENTAL METHODS

3.1 Original Powders

The powders used to fabricate the samples are gas-atomized Inconel 718 powders, supplied by VDM Metals GmbH. The chemical composition is shown in Table 3.1.

Element	***Ni***	***Cr***	***Fe***	***Nb***	***Mo***	***Ti***	***Al***	***Si***
% wt.	53.92	18.32	R17,90	5.20	2.98	0.96	0.54	0.05
Element	***Co***	***C***	***Mn***	***Cu***	***O***	***N***	***S***	
% wt.	0.03	0.024	0.02	0.02	0.008	0.006	< 0.001	

Table 3.1 – Chemical composition of Inconel 718 powders

The particle size in Inconel 718 powders varies, a laser diffraction analysis performed reveals a D10 value of 23 μm, D50 value of 37 μm, and a D90 value of 55 μm.

3.2 Sample Fabrication

The samples were printed using the Laser-Powder Bed Fusion (L-PBF) additive manufacturing technique, with all the specimens fabricated by means of an AconityMIDI device.

3.2.1 AconityMIDI Machine

AconityMIDI machine (Figure 3.1) is a laser-powder bed fusion device used for the fabrication of metallic components starting from powders of weldable materials compatible with this technology. It enables flexibility in the production, process monitoring, and high-temperature platform preheating up to 500°C. The system relies on Aconity Studio Control Software, which allows the modification of all the most important process parameters involved in the printing. Furthermore, the machine itself can be configured with additional tools that can be implemented in order to enhance the process control and of the quality of the final component [93].

In Table 3.2, the key technical specifications and features of the machine are presented:

Build Space	Diameter 170 mm x Height 200 mm
Laser Configuration	Single Mode Fiber 200 W
Optics Configuration / Spot Size	F-Theta / 80 µm 3D Scanning / 80-500 µm
Preheating Temperature / Build Space	500 °C / Ø 170 mm x H 180 mm
Layer Thickness	Down to 10 µm
Max Scan Speed	12 m/s
Inert Gas Type / Pressure	Argon 4.6 / 6 bar Nitrogen / 6 bar Vacuum / < 2 mbar
Inert Gas Consumption	< 5 l/min during process < 60 l/min during purging 0 - 5 l/min for vacuum
Residual Oxygen Content	< 100 ppm
Machine Dimensions (W x D x H)	2450 mm x 1500 mm x 2320 mm
Machine Weight w/o Powder	1450 kg
Applicable Materials	All weldable materials due to freely configurable process parameters

Table 3.2 – AconityMIDI technical sheet [93]

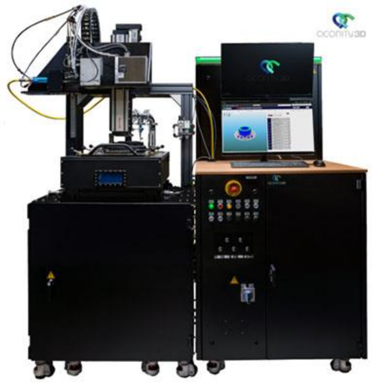

Figure 3.1 – AconityMIDI machine [93]

3.2.2 Characteristics and Parameters of the Specimens

To investigate the influence of platform preheating on the characteristics of the printed alloy, three different temperatures were selected: 80°C, 300°C, and 500°C, each selected according to specific reasons.

- 80°C: Minimum preheating temperature that ensures the production of samples with high density and quality.
- 500°C: Maximum preheating temperature of the platform achievable by AconityMIDI device.
- 300°C: Intermediate temperature, calculated by averaging the aforementioned temperature values and rounding the result to the nearest hundred to simplify machine setup before the printing step.

For each temperature, twenty cubic samples were fabricated across the platform, each characterized by a different combination of scanning speed and laser power. The printed specimens were characterized by a volume of 1 cm^3 (10 x 10 x 10 mm), while other fixed parameters were the layer thickness of 30 μm, the hatching distance of 80 μm, and a 90°/90° scan strategy, hence with a rotation of 90° of the laser path after each layer (Figure 3.3).

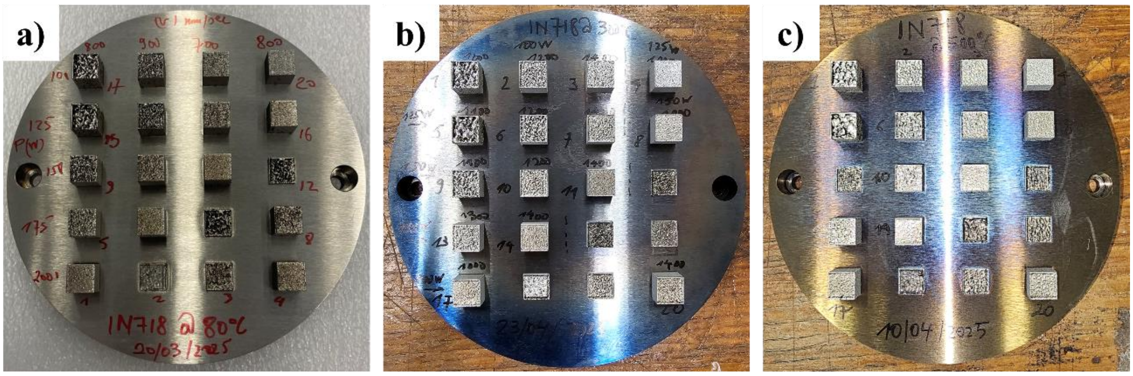

Figure 3.2 – Printed Samples with platform preheating of 80°C (a), 300°C (b), and 500°C (c)

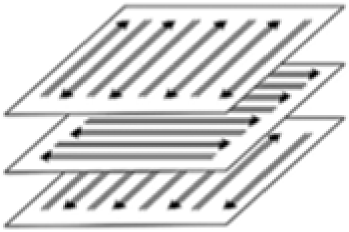

Figure 3.3 – 90°/90° scan strategy [94]

The selection of the optimal combinations of processing parameters to be studied was based on previous studies focused on the characterization of single tracks, keeping just the set of parameters ensuring continuous and uniform tracks. This approach was used for the 80°C and 500°C preheating temperatures. For the intermediate temperature of 300°C, the set of optimal processing parameters was chosen by interpolating between the parameters that yielded the best output quality at 80°C and 500°C, with preference given to combinations that offered higher productivity, thus characterized by higher scanning speed.

In the following tables are presented all the sets of parameters used for each cube fabricated, with the corresponding volumetric energy density (VED), evaluated following the expression presented here.

$$VED = \frac{(Laser\ Power)}{(Layer\ Thickness) * (Hatching\ Distance) * (Scanning\ Speed)} \qquad (4)$$

Sample @ 80°C	**Laser Power [W]**	**Scanning Speed [mm/s]**	**Volumetric Energy Density [J/mm^3]**
1	200	800	104.17
2	200	900	92.59
3	200	700	119.05
4	200	800	104.17
5	175	800	91.15
6	175	900	81.02
7	175	700	104.17
8	175	800	91.15
9	150	800	78.13
10	150	900	69.44
11	150	700	89.29
12	150	800	78.13
13	125	800	65.10
14	125	900	57.87
15	125	700	74.40
16	125	800	65.10
17	100	800	52.08
18	100	900	46.30
19	100	700	59.52
20	100	800	52.08

Table 3.3 – List of process parameters used for the samples fabrication with 80°C preheating, with the samples highlighted in red that are those not fully printed

Sample @ 500°C	**Laser Power [W]**	**Scanning Speed [mm/s]**	**Volumetric Energy Density [J/mm^3]**
1	150	1100	56.82
2	150	1000	62.50
3	125	1200	43.40
4	125	1000	52.08
5	175	1200	60.76
6	175	1100	66.29
7	175	800	91.15
8	150	1200	52.08
9	175	1000	72.92
10	200	900	92.59
11	175	1400	52.08
12	175	1000	72.92
13	200	800	104.17
14	200	1100	75.76
15	200	1000	83.33
16	200	800	104.17
17	200	1400	59.52
18	200	1300	64.10
19	200	1200	69.44
20	200	1400	59.52

Table 3.4 – List of process parameters used for the samples fabrication with 500°C preheating, with the samples highlighted in red that are those not fully printed

Sample @ 300°C	**Laser Power [W]**	**Scanning Speed [mm/s]**	**Volumetric Energy Density [J/mm^3]**
1	100	1000	41.67
2	100	1200	34.72
3	100	1400	29.76
4	125	1000	52.08
5	125	1100	47.35
6	125	1200	43.40
7	125	1400	37.20
8	150	1000	62.50
9	150	1100	56.82
10	150	1200	52.08
11	150	1400	44.64
12	175	1200	60.76
13	175	1300	56.09
14	175	1400	52.08
15	200	800	104.17
16	200	900	92.59
17	200	1000	83.33
18	200	1100	75.76
19	200	1200	69.44
20	200	1400	59.52

Table 3.5 – List of process parameters used for the samples fabrication with 300°C preheating, with the samples highlighted in red that are those not fully printed

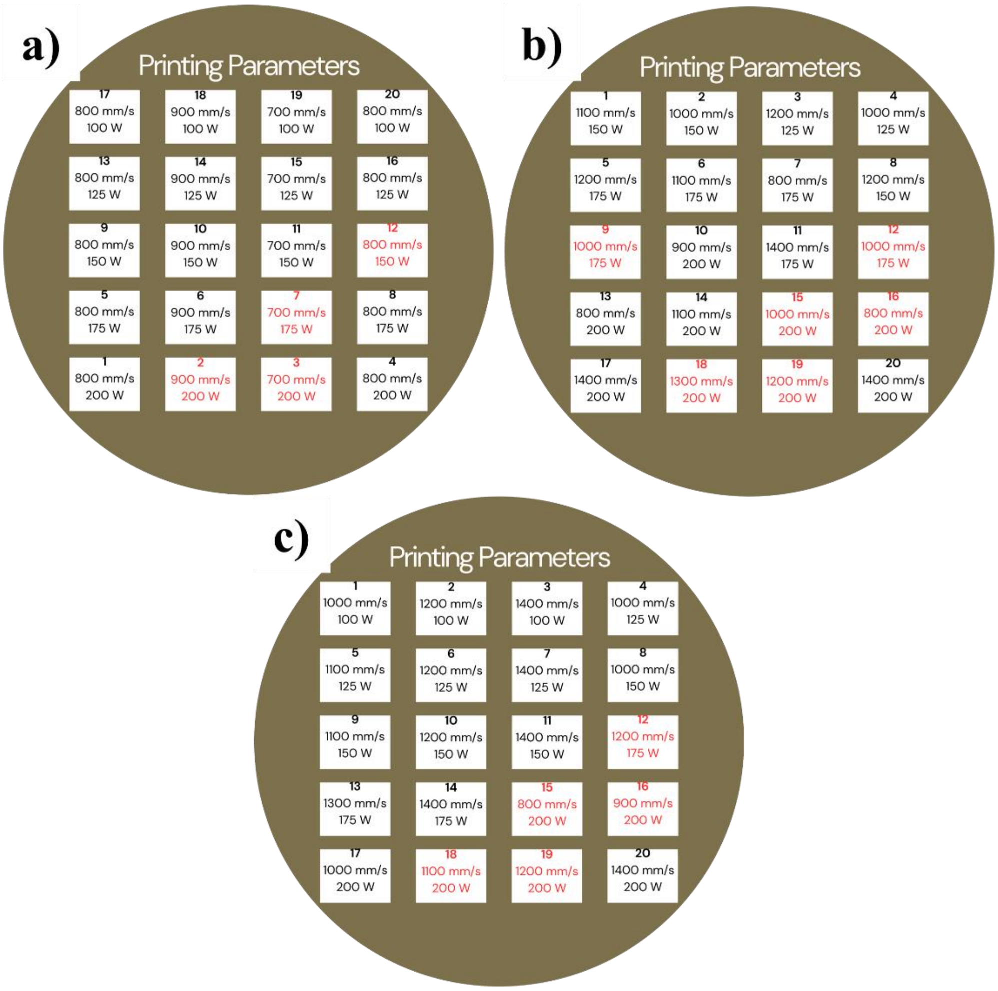
a)
Printing Parameters
17 800 mm/s 100 W
18 900 mm/s 100 W
19 700 mm/s 100 W
20 800 mm/s 100 W
13 800 mm/s 125 W
14 900 mm/s 125 W
15 700 mm/s 125 W
16 800 mm/s 125 W
9 800 mm/s 150 W
10 900 mm/s 150 W
11 700 mm/s 150 W
12 800 mm/s 150 W
5 800 mm/s 175 W
6 900 mm/s 175 W
7 700 mm/s 175 W
8 800 mm/s 175 W
1 800 mm/s 200 W
2 900 mm/s 200 W
3 700 mm/s 200 W
4 800 mm/s 200 W
b)
Printing Parameters
1 1100 mm/s 150 W
2 1000 mm/s 150 W
3 1200 mm/s 125 W
4 1000 mm/s 125 W
5 1200 mm/s 175 W
6 1100 mm/s 175 W
7 800 mm/s 175 W
8 1200 mm/s 150 W
9 1000 mm/s 175 W
10 900 mm/s 200 W
11 1400 mm/s 175 W
12 1000 mm/s 175 W
13 800 mm/s 200 W
14 1100 mm/s 200 W
15 1000 mm/s 200 W
16 800 mm/s 200 W
17 1400 mm/s 200 W
18 1300 mm/s 200 W
19 1200 mm/s 200 W
20 1400 mm/s 200 W
c)
Printing Parameters
1 1000 mm/s 100 W
2 1200 mm/s 100 W
3 1400 mm/s 100 W
4 1000 mm/s 125 W
5 1100 mm/s 125 W
6 1200 mm/s 125 W
7 1400 mm/s 125 W
8 1000 mm/s 150 W
9 1100 mm/s 150 W
10 1200 mm/s 150 W
11 1400 mm/s 150 W
12 1200 mm/s 175 W
13 1300 mm/s 175 W
14 1400 mm/s 175 W
15 800 mm/s 200 W
16 900 mm/s 200 W
17 1000 mm/s 200 W
18 1100 mm/s 200 W
19 1200 mm/s 200 W
20 1400 mm/s 200 W

Figure 3.4 – Distribution of printing parameters for samples printed with 80°C (a), 500°C (b), and 300°C (c) preheating

Samples marked in red in the tables above correspond to those not completely fabricated, as the fabrication process was intentionally stopped due to poor quality that could have compromised the printing of the adjacent cubes. Specifically, the formation of excessive surface roughness or super-elevated edges could have hindered the uniform spreading of the powders across the build platform, thus affecting the quality of successive layers.

Among the successfully fabricated samples, just two cubes per preheating condition were selected for further analyses, other than density assessment, which was, instead, performed on all the samples.

3.2.3 Sample Preparation

The cubes in the as-built conditions are normally bonded to the platform, as no supports were implemented in the printing file, in order to minimize the occurrence of stresses within the structure and to ensure good heat transfer from the preheated platform. As a consequence, the removal of the cubes from the build platform was performed by means of an Electro Discharge Machining (EDM) device, which cuts the samples by generating electrical discharges between an electrode and the workpiece. The cubes in this condition were used for preliminary density analysis performed through a pycnometer, while for the subsequent analyses, the cubes were then cut mechanically in the middle in a direction parallel to the building one, as illustrated in Figure 3.5 – Illustration showing the cutting line, in red, and the building direction of the cubes.

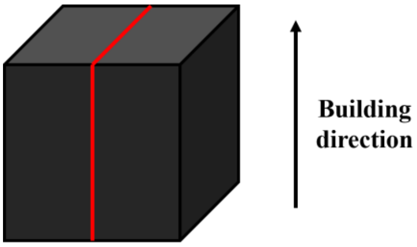

Figure 3.5 – Illustration showing the cutting line, in red, and the building direction of the cubes

Specimens were then mounted in cylindrical bakelite blocks using Struers® Citopress-1 machine (Figure 3.6a), which applies heat and pressure to the bakelite powders, ensuring their polymerization. After the embedding step, the samples were polished down to 1 µm using a Struers® Tegramin-30 polishing machine (Figure 3.6b) to achieve mirror-like and plane surfaces adequate for microscope analysis. This polishing step consists of circular movements of the specimens on a disc of abrasive paper, which progressively removes the more superficial layers.

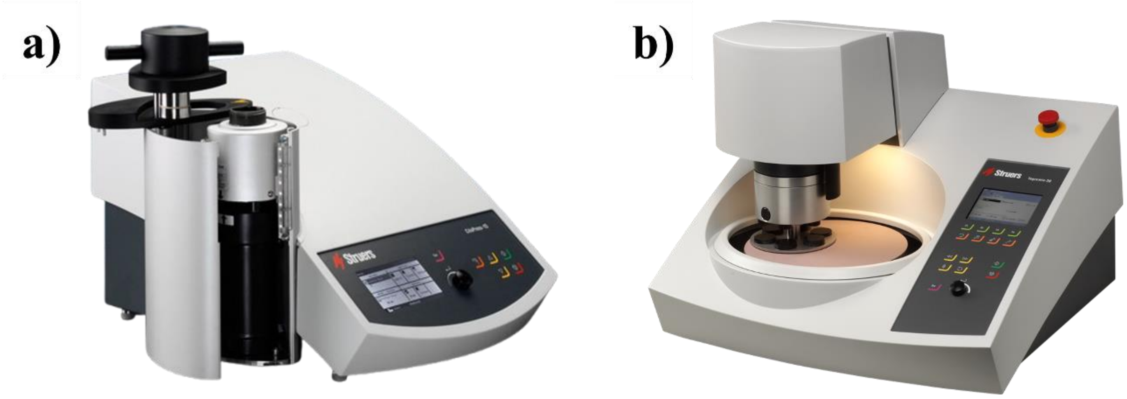

Figure 3.6 – Struers Citopress-1 [95] (a) and Struers Tegramin-30 [96] (b)

Prior to SEM observation, a final polishing with an Oxide Polishing Suspension (OPS), composed of colloidal silica, was performed in order to remove the strain-hardened surface layers and reveal phases and L-PBF-associated features.

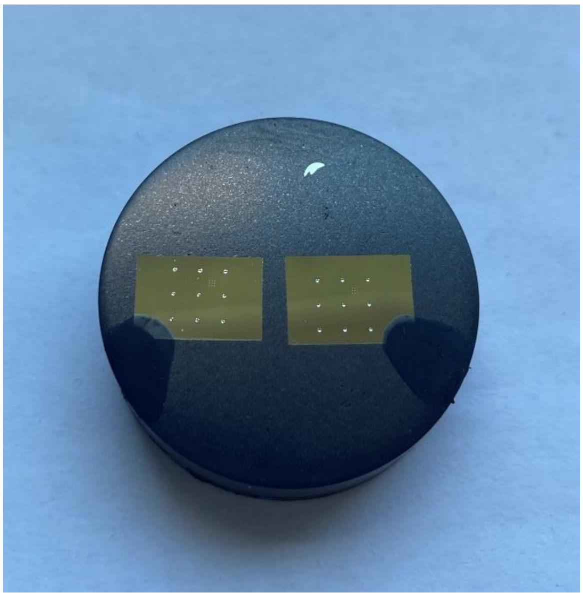

Figure 3.7 – Polished samples after preparation with carbon-based paint and exhibiting hardness indentations

3.3 Microstructural Characterization

The microstructural characterization of the cubes was performed using both Optical Microscope (OM) and Scanning Electron Microscope (SEM).

3.3.1 Optical Microscope (OM) and ImageJ Analysis

The sections of the polished samples were examined by means of an Olympus® BX60 microscope (Figure 3.8) at 2.5x, 5x, and 10x magnifications, while overview pictures of the entire cross-section were taken, with a 2.5x magnification, using Olympus Stream Analysis® Software, which allows image acquisition and processing.

Figure 3.8 – Olympus BX60 microscope [97]

3.3.2 Scanning Electron Microscope (SEM)

Samples with the highest density were observed using Tescan® Clara Ultra-High Resolution SEM (Figure 3.9), allowing a more detailed analysis thanks to its capability to achieve much greater magnifications. Before imaging, the selected specimens were first polished with a colloidal silica suspension and then mounted on appropriate sample holders. To prevent issues of charge accumulation during imaging, the surface of each specimen was connected to the sample holder by means of a carbon-based conductive paint, which permitted charge dissipation (Figure 3.7).

The observations of the surface and of the defects present on the surface of the samples were performed using both Secondary Electrons (SE) and Back-Scattered Electrons (BSE) detectors. The combination of the two permitted gathering more precise information about the observed surface. From each sample, micrographs of different regions, in particular those presenting defects or inclusions, were taken with magnifications of 300x, 3000x, and 10,000x.

To complete the SEM analysis, Bruker® Energy Dispersive Spectroscopy (EDS) was also performed to better understand the distribution of elements throughout different regions of the cross-section of the samples, with particular focus on the regions close to defects and inclusions to better characterize them.

Figure 3.9 – Tescan Clara Ultra-High Resolution SEM [98]

3.4 Density Measurements

The evaluation of the density of all the samples was performed preliminarily with a pycnometer in order to have a general overview of the quality of each cube, and subsequently by analyzing the optical micrographs through appropriate software.

Different measurement approaches give distinct definitions of density. In particular, it is possible to distinguish between:

- True density, which refers to the density of the solid material itself, excluding any contribution from porosity, voids, or cracks that may be present. It is typically obtained by techniques such as gas pycnometry.
- Apparent density, which is a measure accounting for the volume of the material together with eventual closed voids that may be present within the solid. This is calculated with techniques such as Archimedes' method.
- Measured density, corresponding with the density evaluated from micrographs, where the total surface area of the porosities is subtracted from the bulk material area.

3.4.1 Density Assessment with Pycnometer

A first assessment of the density of the as-built cubes was performed through AccuPyc® II Series 1345 gas pycnometer (Figure 3.10). This non-destructive method for density measurement uses an inert gas that fills the chamber in which the sample is contained. By knowing the mass of the sample and evaluating the gas displacement, the device is able to determine the density of the analyzed specimen. For increased accuracy, the machine repeats the measurement five times for each sample, and the density is taken as the average of the results given by the device.

micromeritics
AccuPyc II 1345
Gas Pycnometer

Figure 3.10 – AccuPyc II Serie 1345 Pycnometer [99]

3.4.2 Density Measurement with Micrographs

Since the accuracy of the pycnometer can be affected by the presence of closed porosities, which are not filled by the gas, the assessment of the density was also carried out by analyzing micrographs obtained with the optical microscope.

The overview pictures of each specimen, corresponding to a vertical cross-section parallel to the building direction, taken with a magnification of 2.5x with the optical microscope, were examined through ImageJ® software (Figure 3.11 – Example of thresholding performed with ImageJ® software for the evaluation of the density). On the acquired greyscale micrographs, a threshold value was applied to distinguish porosities (dark regions) from dense material (light regions), allowing the evaluation of the area of pores.

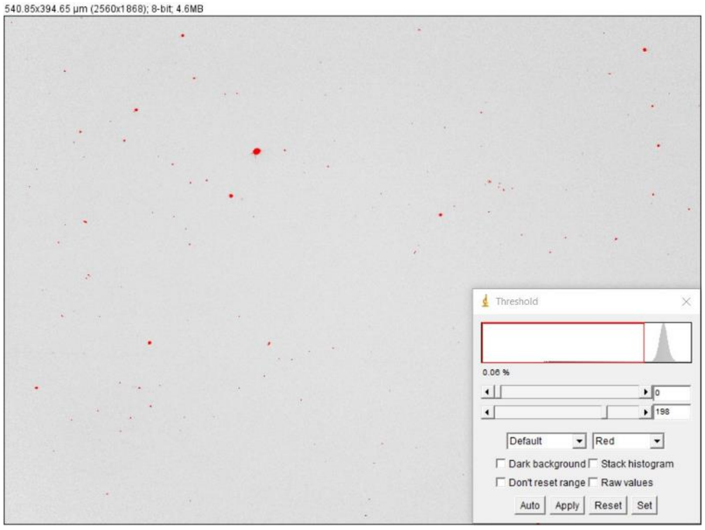
540.85x394.65 µm (2560x1868); 8-bit; 4.6MB
Threshold
0.06 %
0
198
Default
Red
☐ Dark background
☐ Stack histogram
☐ Don't reset range
☐ Raw values
Auto
Apply
Reset
Set

Figure 3.11 – Example of thresholding performed with ImageJ® software for the evaluation of the density

By comparing the surface area of porosities and the total area observed, it was possible to estimate the density value for each specimen.

3.5 Hardness Tests

On the samples with the highest quality, an evaluation of macro-hardness and micro-hardness was also performed.

3.5.1 Macro-Hardness and Micro-Hardness

The indentations performed for the evaluation of the hardness of the samples were obtained using a Falcon 500G2 machine by Innovatest (Figure 3.12), equipped with an electronic cell force and a closed-loop regulation. Such a device is made of an automatic system that permits the exchange between lenses and indenter, supports a fully automated test cycle, and provides automatic lens focusing. The machine allows, in addition, automatic image evaluation to establish the value of hardness for each indentation. The location of each indentation was manually set to form a grid pattern, and the indenter used was a Vickers-type [100].

In macro-hardness testing, a grid of 9 different indentations covering 6x6 mm of the cross-section was set, with each point separated from the adjacent one by a distance of 3 mm. Vickers macro-hardness tests were performed by using a load of 10 kgf (HV10).

For micro-hardness, instead, a smaller grid of 9 points, distanced 0.3 mm from each other and appropriately distanced from macro-hardness indentations, was used. The location of this smaller grid remained consistent in each sample tested. In particular, this smaller grid was defined within the top right quadrant obtained by the macro-hardness grid (Figure 3.13). The load used for micro-hardness Vickers indentations was 300 gf (HV0.3).

INNOVATEST

Figure 3.12 – Innovatest Falcon 500G2 hardness tester [100]

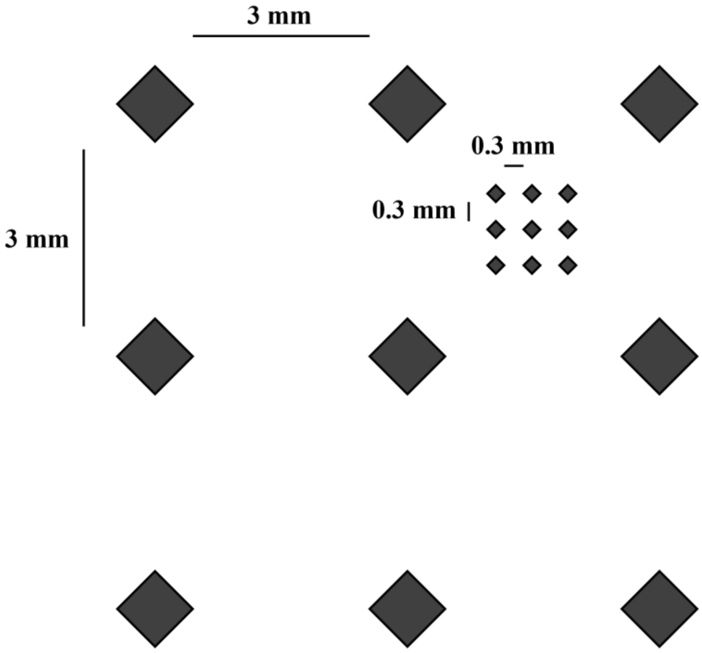

Figure 3.13 – Schematic of indentation grid for macro-hardness and micro-hardness

Chapter 4

RESULTS

4.1 Density Assessment

4.1.1 Pycnometer Density

A preliminary evaluation of the "true" density of the as-built cubes was performed by using a gas pycnometer. The obtained values allowed us to identify the samples with the highest quality and also to start drafting the processing maps correlating sample quality with the process variables.

The true density results provided by the pycnometer were expressed in g/cm^3; thus, for facilitating comparison with the densities obtained by micrograph analysis, the values were converted into density percentage by comparing the true density with the typical density of Inconel 718 alloy ((5), which is 8.24 g/cm^3.

$$\%\,\boldsymbol{Density} = \frac{\boldsymbol{\rho \cdot 100}}{\boldsymbol{\rho_{bulk}}} \tag{5}$$

For all platform preheating conditions, the measured true densities of all the samples exceeded 95 %, with the only exception of sample 9 printed at 80°C, which exhibited a slightly lower density. The data about density obtained through the gas pycnometer are presented in Tables Table 4.1, Table 4.2, and Table 4.3.

Sample @ 80°C	**Laser Power [W]**	**Scanning Speed [mm/s]**	**VED [J/mm^3] (*(4)*)**	**Density [g/cm^3]**	**Density [%]**
1	200	800	104.17	8.23	99.82
4	200	800	104.17	8.21	99.65
5	175	800	91.15	8.14	98.79
6	175	900	81.02	8.22	99.71
8	175	800	91.15	8.14	98.80
9	150	800	78.13	7.82	94.86
10	150	900	69.44	8.09	98.22
11	150	700	89.29	8.20	99.57
13	125	800	65.10	8.08	98.05
14	125	900	57.87	8.09	98.19
15	125	700	74.40	8.02	97.35
16	125	800	65.10	8.17	99.14
17	100	800	52.08	8.09	98.17
18	100	900	46.30	8.14	98.80
19	100	700	59.52	7.98	96.89
20	100	800	52.08	8.10	98.31

Table 4.1 – Pycnometer density for the samples printed with 80°C preheating

Sample @ 300°C	Laser Power [W]	Scanning Speed [mm/s]	VED [J/mm^3] ((*4*)	Density [g/cm^3]	Density [%]
1	100	1000	41.67	8.07	97.94
2	100	1200	34.72	8.16	98.98
3	100	1400	29.76	7.96	96.58
4	125	1000	52.08	8.21	99.58
5	125	1100	47.35	8.08	98.01
6	125	1200	43.40	7.93	96.30
7	125	1400	37.20	8.10	98.36
8	150	1000	62.50	8.19	99.41
9	150	1100	56.82	7.88	95.67
10	150	1200	52.08	8.16	99.07
11	150	1400	44.64	8.21	99.62
13	175	1300	56.09	8.16	99.03
14	175	1400	52.08	8.20	99.47
17	200	1000	83.33	8.19	99.43
20	200	1400	59.52	8.21	99.59

Table 4.2 – Pycnometer density for the samples printed with 300°C preheating

Sample @ 500°C	**Laser Power [W]**	**Scanning Speed [mm/s]**	**VED [J/mm^3] ((*4*))**	**Density [g/cm^3]**	**Density [%]**
1	150	1100	56.82	8.10	98.30
2	150	1000	62.50	8.07	97.90
3	125	1200	43.40	7.95	96.51
4	125	1000	52.08	7.99	97.01
6	175	1200	66.29	8.27	100.33
7	175	1100	91.15	8.08	98.01
8	175	800	52.08	8.21	99.66
10	200	900	92.59	8.14	98.74
11	175	1400	52.08	8.21	99.67
13	200	800	104.17	8.17	99.19
14	200	1100	75.76	8.23	99.88
17	200	1400	59.52	8.23	99.88
20	200	1400	59.52	8.21	99.62

Table 4.3 – Pycnometer density for the samples printed with 500°C preheating

4.1.2 Density Measurement through Micrographs

To get a more accurate estimation of the cubes' densities, the micrographs of the cross-section of the specimens were analyzed using ImageJ® software. This method allowed the definition of the total porosity area, from which the density was calculated. Moreover, the analysis permitted the recording of individual pore sizes on the surface.

The results are presented in Tables Table 4.4, Table 4.5, and Table 4.6, along with graphs illustrating the correlation between measured density and volumetric energy density (VED).

Sample @ 80°C	Laser Power [W]	Scanning Speed [mm/s]	VED [J/mm^3] (*(4)*)	Density [%]
1	**200**	**800**	**104.17**	**99.88**
4	**200**	**800**	**104.17**	**99.92**
5	175	800	91.15	98.84
6	**175**	**900**	**81.02**	**99.95**
8	175	800	91.15	98.10
9	150	800	78.13	91.98
10	150	900	69.44	97.68
11	150	700	89.29	99.65
13	125	800	65.10	85.16
14	125	900	57.87	88.62
15	125	700	74.40	97.13
16	125	800	65.10	99.30
17	100	800	52.08	97.47
18	100	900	46.30	83.88
19	100	700	59.52	92.89
20	100	800	52.08	92.27

Table 4.4 – Density measured from micrographs for samples printed with 80°C preheating. Values highlighted in green correspond to samples with a density higher than 99.7%.

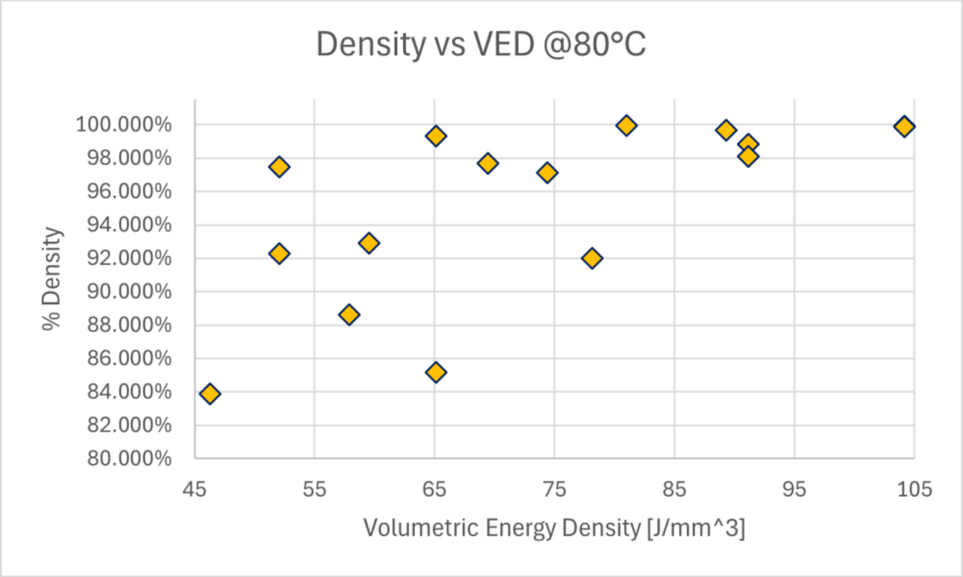

Figure 4.1 – Variation of sample density as a function of VED for specimens printed with 80°C preheating

Sample @ 300°C	Laser Power [W]	Scanning Speed [mm/s]	VED [J/mm^3] ((*4*))	Density [%]
1	100	1000	41.67	82.30
2	100	1200	34.72	85.67
3	100	1400	29.76	96.16
4	125	1000	52.08	96.19
5	125	1100	47.35	90.41
6	125	1200	43.40	97.07
7	125	1400	37.20	98.73
8	**150**	**1000**	**62.50**	**99.90**
9	150	1100	56.82	93.28
10	150	1200	52.08	98.98
11	**150**	**1400**	**44.64**	**99.93**
13	175	1300	56.09	99.40
14	**175**	**1400**	**52.08**	**99.98**
17	**200**	**1000**	**83.33**	**99.96**
20	**200**	**1400**	**59.52**	**99.94**

Table 4.5 – Density measured from micrographs for samples printed with 300°C preheating. Values highlighted in green correspond to samples with a density higher than 99.7%.

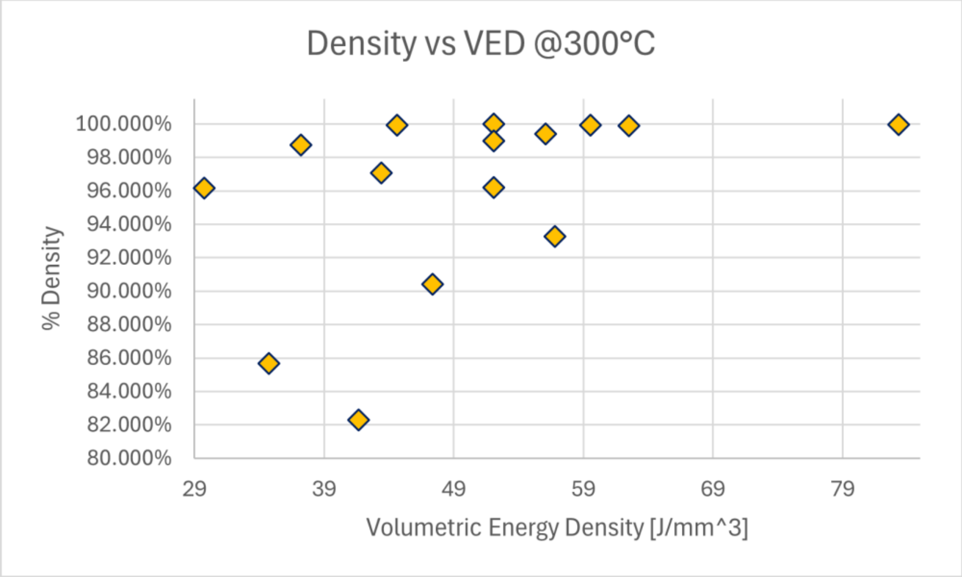

Figure 4.2 – Variation of sample density as a function of VED for specimens printed with 300°C preheating

Sample @ 500°C	**Laser Power [W]**	**Scanning Speed [mm/s]**	**VED [J/mm^3] (*(4)*)**	**Density [%]**
1	150	1100	56.82	84.15
2	150	1000	62.50	85.56
3	125	1200	43.40	95.35
4	125	1000	52.08	96.38
6	175	1200	66.29	92.18
7	175	1100	91.15	98.63
8	**175**	**800**	**52.08**	**99.72**
10	200	900	92.59	97.90
11	**175**	**1400**	**52.08**	**99.81**
13	200	800	104.17	98.50
14	**200**	**1100**	**75.76**	**99.86**
17	200	1400	59.52	99.64
20	**200**	**1400**	**59.52**	**99.72**

Table 4.6 – Density measured from micrographs for samples printed with 500°C preheating. Values highlighted in green correspond to samples with a density higher than 99.7%.

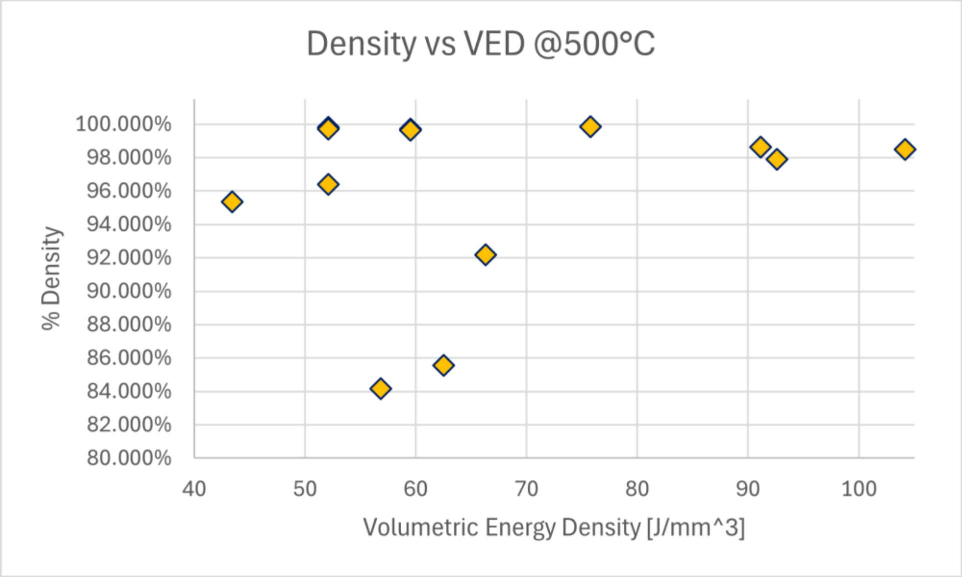

Figure 4.3 – Variation of sample density as a function of VED for specimens printed with 500°C preheating

The measured density is observed to increase with increasing volumetric energy density (VED), particularly for preheating temperatures of 80°C and 300°C. At 500°C, however, this trend is less pronounced, and the density slightly decreases at the highest VED used.

The correlation between measured density and volumetric energy density of each sample reveals different optimal ranges for VED depending on the platform preheating condition used:

- At 80°C, the optimal energy density is significantly higher, spanning between 80 and 105 J/mm^3.
- At 300°C, the optimal VED ranges over a broader interval between 45 and 85 J/mm^3.
- At 500°C, the range is similar to that of 300°C but narrower, as the one obtained at 80°C. The optimal energy density spans from 50 to 75 J/mm^3.

This shift in the optimal VED range with preheating temperature can be clearly observed in Figure 4.4 – Variation of the optimal VED range for the different preheating temperatures.

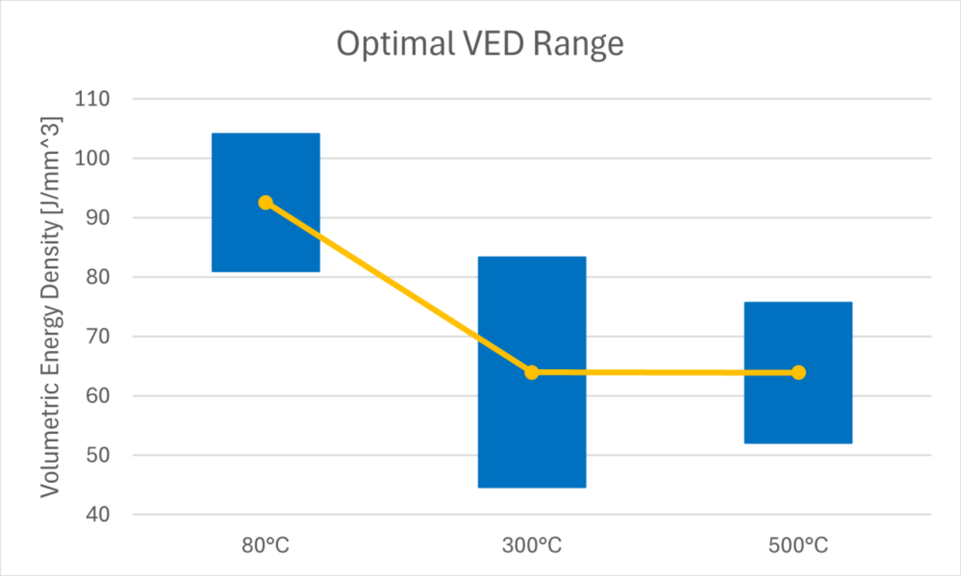

Figure 4.4 – Variation of the optimal VED range for the different preheating temperatures

4.1.3 Processing Maps

Figure 4.5 shows the process maps corresponding to the three different platform preheating temperatures, where the best samples with the best measured density are highlighted in green, while the specimens that were not successfully printed are marked with red crosses.

From the charts, it can be seen that, regardless of the preheating temperature, specimens with the highest measured density (greater than 99.5%) are primarily located in the regions characterized by a greater volumetric energy density, which is directly proportional to laser power and inversely proportional to scanning speed. Conversely, the partially printed specimens were typically associated with the highest laser powers among those used.

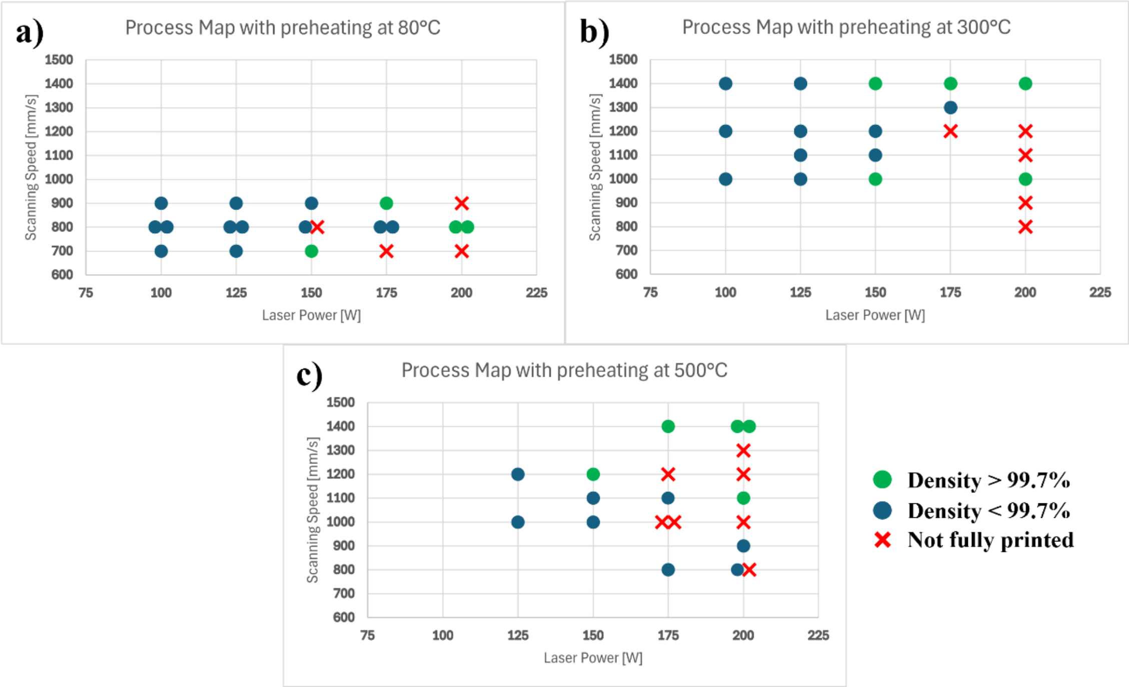

Figure 4.5 – Process map for 80°C (a), 300°C (b), and 500°C (c) platform preheating

Based on the density results that were obtained and the critical size of the defects (discussed in chapter 4.2.2 Porosity Critical Size), a subset of two samples for each preheating temperature was selected to undergo further analyses. These additional investigations included SEM observations, EDX analysis, and hardness measurements. The selected specimens are those summarized in Table 4.7.

Preheating Temperature	**Sample No.**	**Laser Power [W]**	**Scanning Speed [mm/s]**	**VED [J/mm^3] ((*4*))**	**Designation**
80°C	4	200	800	104.17	***80-S4***
	6	175	900	81.02	***80-S6***
300°C	14	175	1400	52.08	***300-S14***
	17	200	1000	83.33	***300-S17***
500°C	14	200	1100	75.76	***500-S14***
	20	200	1400	59.52	***500-S17***

Table 4.7 – List of the samples selected for further analyses

4.2 Internal Defects

4.2.1 Porosity Morphologies

The porosities detected on the different samples exhibited different dimensions and, in particular, different morphologies, which are closely related to the specific mechanism responsible for their formation.

The most diffused pore type identified within the analyzed samples was gas porosity. These kinds of defects are typically small in size compared to other porosity types and originate from the entrapment of gases during the solidification of the melt pool. Gas pores generate defects that are generally highly spherical, as illustrated in Figure 4.6.

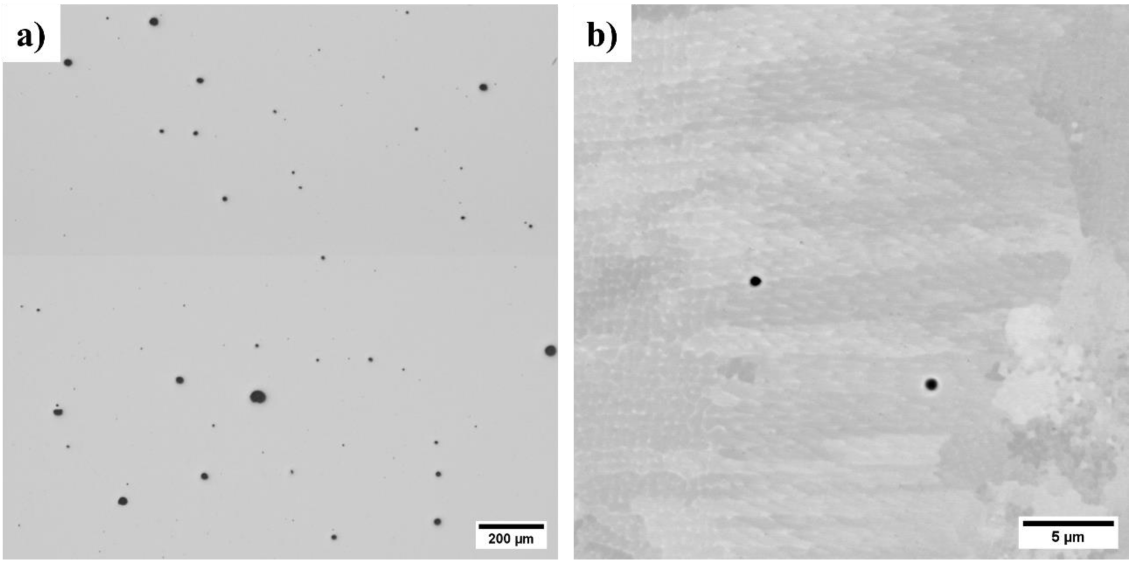

Figure 4.6 – Gas porosity morphology observed with an optical microscope at 2.5x magnification (a) and with SEM at 300x magnification (b)

A certain degree of deviation from perfect circularity of gas porosities was observed at higher magnifications with SEM micrographs. In several cases, material protrusions were observed growing towards the inside of the porosity. The small features detected around these porosities were not correlated with any element peak in EDX profiles (Figure 4.7b), confirming that they are simply portions of the original pore partially filled by the ingrowing material.

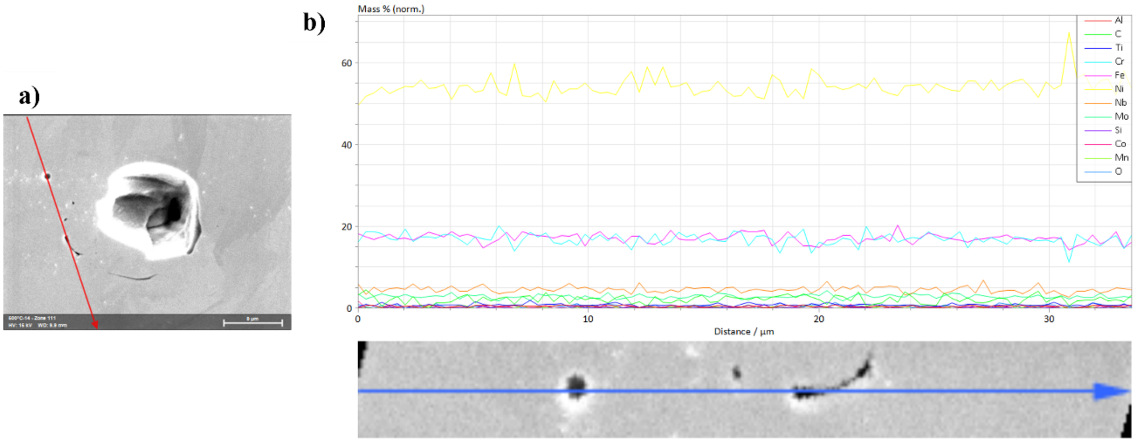

Figure 4.7 – SEM micrograph showing the selected EDX line for the analysis of some features observed close to a porosity (a) and the corresponding mass percentage profile of the elements along the line (b)

In specimens with the lowest quality, the predominant porosity type was, instead, lack-of-fusion (LOF) porosity. These defects typically exhibit geometries that are more elongated and irregular, and in some cases enclose unmelted powders (Figure 4.8b). As illustrated in Figure 4.8, LOF defects can reach considerable dimensions when the combination of process parameters is not good.

LOF porosities were primarily detected in the samples fabricated with the lowest volumetric energy densities for each platform preheating temperature. Such low-energy conditions are associated with the combination of low laser power and high scanning speed, which prevents complete fusion between adjacent layers.

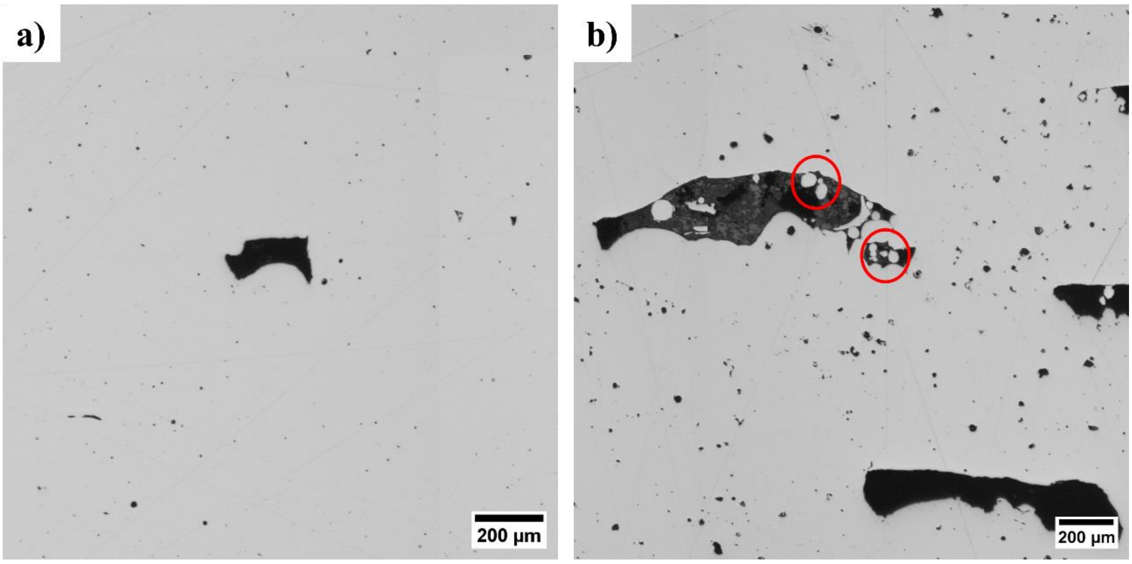

Figure 4.8 – Lack-of-fusion porosity morphology at 2.5x magnification (a), with unmelted particles highlighted in red (b)

Finally, in the surface layers of some cubes, the presence of spatter particles was highlighted, often accompanied by entrapped porosities located just beneath these protrusions (Figure 4.9). Spatters are molten metal droplets ejected from the melt pool during processing, which solidify in flight and subsequently redeposit on the surface of the material. Their presence can affect subsequent layer deposition and promote the formation of defects during the following laser scans.

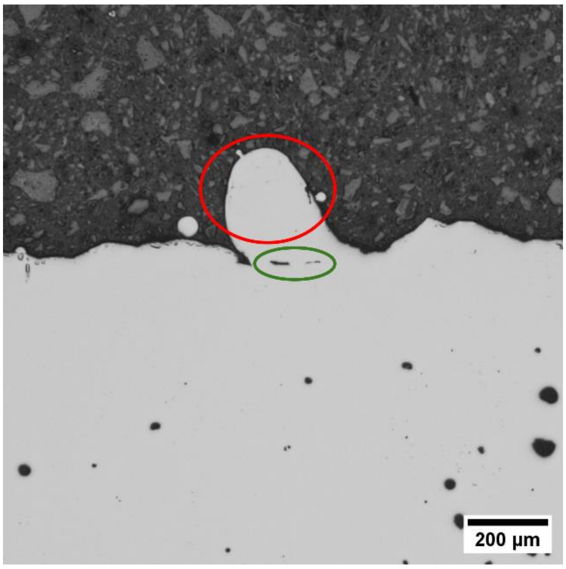

Figure 4.9 – Spatter particle, highlighted in red, on the surface of a sample, with the corresponding underlying defects indicated in green

4.2.2 Porosity Critical Size

The density of the fabricated cubes is not sufficient to fully establish the quality of the specimens; it is also fundamental to evaluate the sizes of the largest pores.

During the micrograph-based density analysis, the area of every porosity in each sample was recorded. This made it possible to evaluate an equivalent diameter for the pores, which can then be compared to a critical threshold to determine whether they might affect the mechanical properties of the component. For this purpose, the estimation of the equivalent diameter is based on (6).

$$\boldsymbol{D_{eq} = 2\sqrt{\frac{A}{\pi}}} \tag{6}$$

The data about the size of the largest pores detected in each sample are summarized in Table 4.8 – Equivalent diameter of the largest porosity in each printed sample for the three different preheating temperatures.

Sample @80°C	Defect Size [µm]	Sample @300°C	Defect Size [µm]	Sample @500°C	Defect Size [µm]
1	71	1	1277	1	1149
4	36	2	841	2	805
5	309	3	339	3	315
6	35	4	217	4	185
8	481	5	967	6	596
9	670	6	87	7	279
10	391	7	274	8	321
11	285	8	205	10	501
13	1127	9	688	11	50
14	759	10	272	13	353
15	381	11	35	14	62
16	391	13	274	17	329
17	438	14	31	20	71
18	750	17	30	-	-
19	378	20	50	-	-
20	301	-	-	-	-

Table 4.8 – Equivalent diameter of the largest porosity in each printed sample for the three different preheating temperatures

The equivalent diameters of the largest pores in each sample were all greater than 30 µm. Under preheating conditions of 80°C and 300°C, the smallest critical defects exhibited restrained dimensions below 40 µm, whereas for the 500°C preheating condition, the best sample still presented the largest pore of 50 µm.

4.2.3 Hot Cracks

The analysis at higher magnifications carried out with SEM revealed the presence of some hot cracks (Figure 4.10 – SEM micrograph, with 300x magnification, showing a hot crack (a) and atomic percentage profile of the elements along an EDX line passing through the crack (b)a), which formed during the solidification stage of the alloy. To further investigate these defects, an EDX line profile was acquired across one of these cracks, in order to assess any possible segregation of elements along its path. The analysis showed no detectable variation in chemical composition in correspondence with the crack (Figure 4.10b).

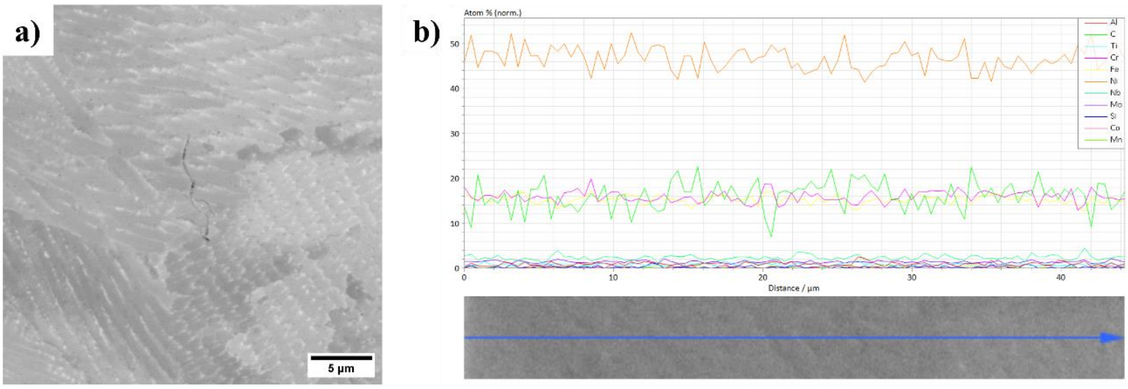

Figure 4.10 – SEM micrograph, with 300x magnification, showing a hot crack (a) and atomic percentage profile of the elements along an EDX line passing through the crack (b)

4.3 Microstructure

4.3.1 Cellular Structure

One of the most distinctive microstructural features revealed through the combination of OPS polishing and SEM observation is the typical cellular structure of L-PBF Inconel 718. In Figure 4.11, it is possible to observe the cells, constituting the grains of the alloy, whose morphology depends on the orientation of the subgrains with respect to the surface of the cross-section.

The analysis of the micrographs obtained for all the analyzed samples allowed a general estimation of the subgrain sizes. On average, the cellular structure exhibits subgrains with sizes of approximately 0.5 microns for all the samples, with some cells reaching dimensions up to 1 micron. No significant variations were highlighted among specimens fabricated at different preheating conditions.

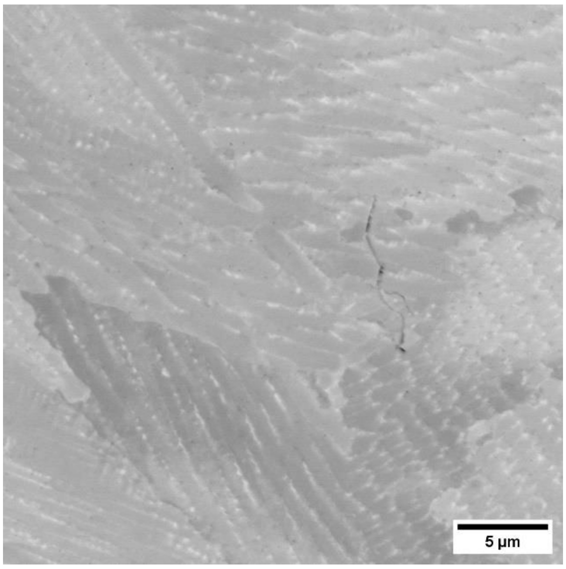

Figure 4.11 – Micrograph showing the cellular structure of L-PBF Inconel 718

4.3.2 Oxide Inclusions

To investigate the possible presence of secondary phases, the selected specimens were examined using EDX analysis, which allowed the evaluation of the chemical elements' distribution. An initial mapping of the elements (Figure 4.12) was performed in a region not presenting any observable feature, revealing an overall chemical uniformity throughout the matrix. This observation suggests the absence of significant element segregation within the bulk alloy, which could be associated with the limited spatial resolution of EDX.

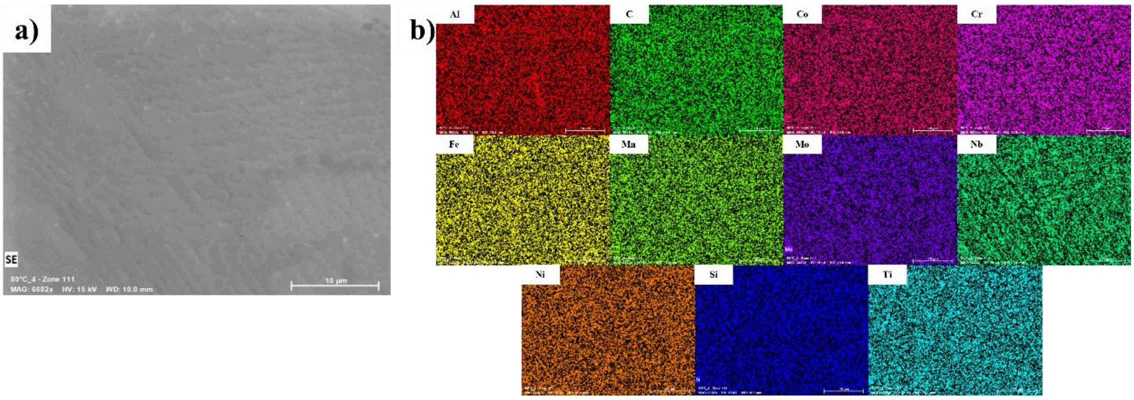

Figure 4.12 – SEM micrograph of the analyzed region (a) and EDX mapping of the elements (b)

Subsequent EDX investigations on the selected specimens were then focused on line profiles across defects and inclusions to achieve a more detailed chemical characterization of them. The oxide inclusions observed across the different samples exhibited two distinct morphologies: some appeared as discontinuous and irregular (Figure 4.13a) in shape, while others were instead smoother and sharp-edged (Figure 4.13b).

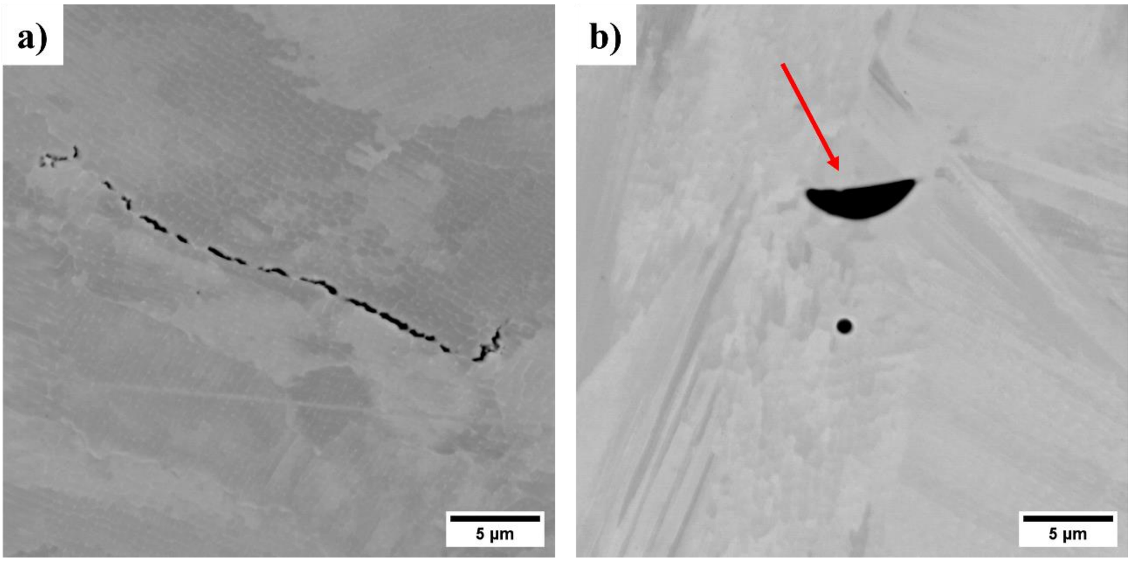

Figure 4.13 – SEM micrographs showing irregular (a) and sharp-edged inclusions, indicated with the red arrow (b)

The EDX line profile analysis of these oxide inclusions revealed different chemical compositions associated with the two different morphologies. The irregular inclusions, in many cases located in proximity to porosity sites, exhibited a high content of Si and O, indicating they are silica (SiO_2) inclusions. This can be observed by the peaks for Si and O elements in the EDX profiles (Figure 4.14b).

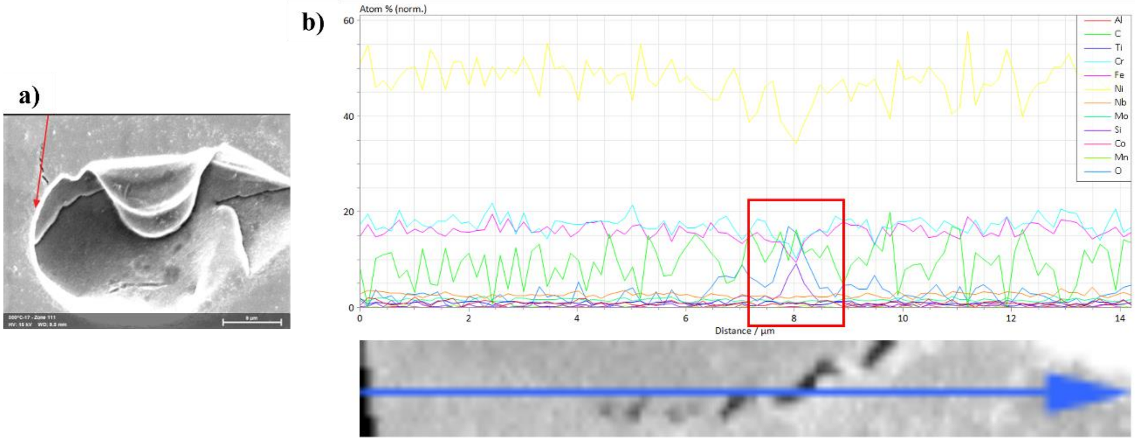

Figure 4.14 – SEM micrograph showing the selected EDX line for the analysis of an irregular inclusion (a) and the corresponding atomic percentage profile of the elements along the line (b), with the red box highlighting Si and O peaks

Conversely, the sharp inclusions were found to be rich in Al, O, and Ti, suggesting the formation of mixed oxides combining the presence of both Al and Ti. In this case, the EDX profiles clearly display peaks for Al and O elements, accompanied by a smaller Ti peak, as can be seen from Figure 4.15b.

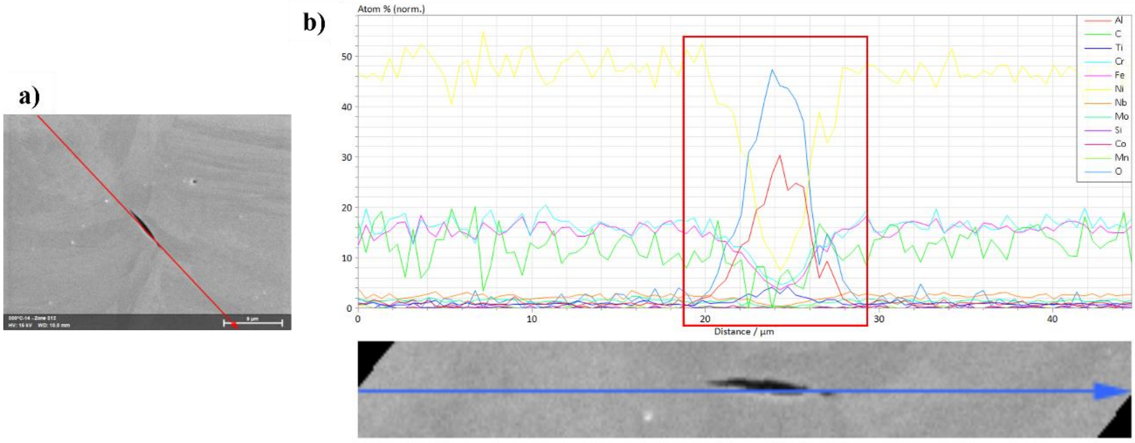

Figure 4.15 – SEM micrograph showing the selected EDX line for the analysis of a sharp-edged inclusion (a) and the corresponding atomic percentage profile of the elements along the line (b), with the red box highlighting Al, O, and Ti peaks

4.4 Mechanical Characterization

4.4.1 Macro and Micro Hardness

The macroscopic Vickers hardness tests, carried out with a load of 10 kgf (HV10), yielded hardness values ranging from 295 to 325 HV. As illustrated in the chart in Figure 4.16, the highest hardness was generally measured for the samples fabricated with the lowest preheating temperature, whereas the samples produced under higher platform temperatures, 300°C and 500°C, exhibited comparable hardness levels.

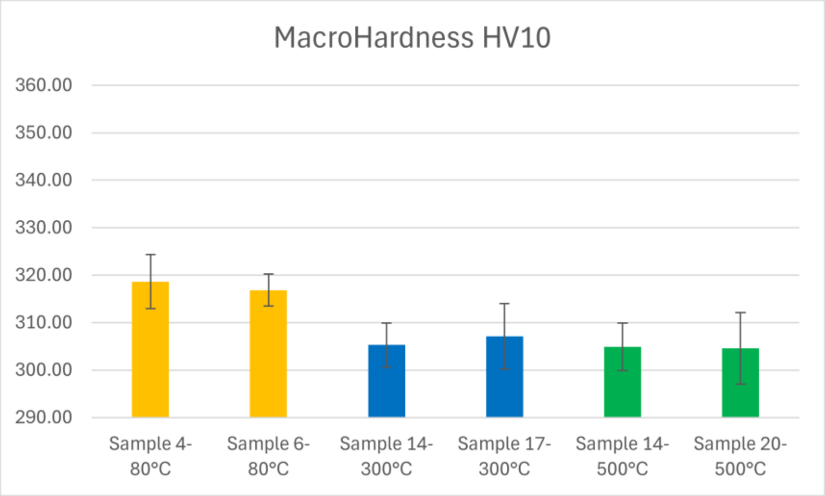

Figure 4.16 – Macroscopic hardness results of the analyzed samples

The microscopic Vickers hardness analysis, performed with a load of 300 gf (HV0.3), provided significantly higher hardness values than the macro-hardness tests. Moreover, the trend observed in HV10 tests was not completely replicated at the microscale: the samples fabricated with 80°C preheating again showed higher hardness than those printed at 300°C, while the two analyzed samples produced with 500°C preheating displayed more variable results. Specifically, sample 500-S14 was characterized by a hardness slightly above that of the 300°C specimens, while sample 500-S20, in some cases, reached values exceeding even those of the samples printed with 80°C platform preheating.

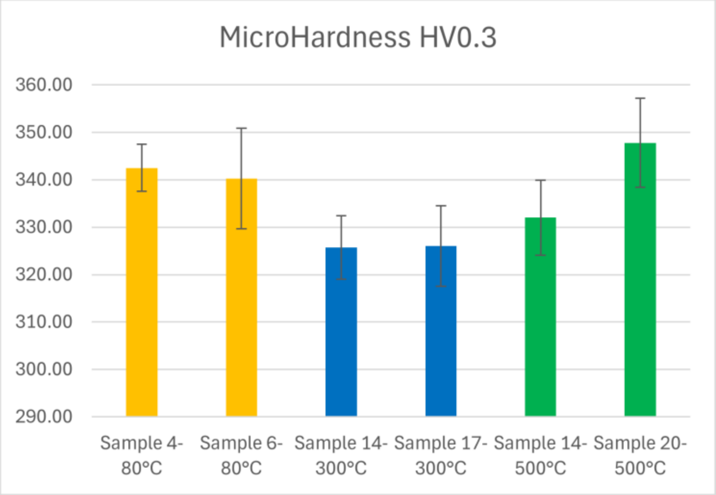

Figure 4.17 – Microscopic hardness results of the analyzed samples

Sample	*HV10*	*Standard Deviation*	*Sample*	*HV0.3*	*Standard Deviation*
80-S4	318.63	5.73	**80-S4**	342.52	4.99
80-S6	316.84	3.37	**80-S6**	340.23	10.61
300-S14	305.27	4.62	**300-S14**	325.67	6.69
300-S17	307.09	6.91	**300-S17**	326.02	8.46
500-S14	304.87	5.03	**500-S14**	332.01	7.89
500-S20	304.54	7.52	**500-S20**	347.80	9.40

Table 4.9 – Macro hardness and micro hardness average values for each sample

Chapter 5

DISCUSSION

5.1 Limitations of VED and Effect of Preheating on Process Map and Output Quality

In additive manufacturing technologies such as laser-powder bed fusion (L-PBF), which was the technique used for fabricating the samples in this study, the mechanical properties of the printed components are strongly influenced by the process parameters, whose effect is closely related to the volumetric energy density (VED) [14], [101]. Achieving high-quality components, therefore, requires the definition of an optimal process window encompassing the most suitable combination of parameters [3]. To establish this window, it is essential to investigate the as-built specimens.

In this study, the quality of the fabricated samples was evaluated under three different platform preheating temperatures to investigate their influence on the mechanical properties of the printed components. For each preheating condition, a total of 20 samples were produced using two variable parameters — laser power (P) and scanning speed (v_s) — whereas layer thickness and hatching distance were kept constant. Because the effect of preheating on the energy input per unit volume is indirect and complex, the preheating temperature is normally not taken into account in the general VED equation [4]. Consequently, VED is conventionally expressed only as a function of the variables P and v_s.

Most of the cubes were successfully printed and subsequently evaluated in terms of density, defect type and size, inclusion content, and hardness. However, a few specimens experienced a premature build interruption due to process conditions that did not ensure their proper fabrication, nor that of the adjacent cubes.

The analysis of the prematurely stopped during the fabrication revealed that they were concentrated in the region of high laser powers, specifically above 175 W. This behavior can be attributed to the transition from conduction to keyhole melting mode, occurring at high VEDs, where the turbulence of the melt pool increases, favoring the insurgence of defects in the alloy [31].

The excessive energy input responsible for the turbulence can result in the entrapment of gases during solidification, as well as surface swelling, where material locally rises out of the printing plane, hindering uniform powder spreading of subsequent layers [102]. In addition, high turbulence promotes the ejection of spatters, which are typically larger than the powders constituting the bed. When redeposited, these particles may not fully melt during successive laser scans, leading to increased roughness [103]. It is also noteworthy that spatters can affect adjacent cubes. This can help explain why some cubes with only moderate VED values still require premature interruption.

On the other hand, low laser powers, and therefore reduced volumetric energy density, were associated with the formation of specimens exhibiting the lowest densities, primarily due to the development of lack-of-fusion porosities. When insufficient laser power is combined with high scanning speeds, the powder layer is not completely melted during the laser scan, preventing proper bonding between adjacent layers and causing the formation of large and irregular porosities [14].

When comparing the three preheating temperatures investigated, increasing the platform temperature from 80°C to 300°C resulted in a higher number of specimens with measured densities exceeding 99.5%. Conversely, with a preheating of 500°C, the optimal processing window narrowed again, and the samples fabricated at this preheating temperature failed to achieve measured densities above 99.9%, in contrast with the other preheating conditions. In addition, they exhibited gas porosities that were both more numerous and larger. This is also highlighted by the data on maximum pore size, which show values of at least 50 microns for these samples. Preheating generally reduces the solidification rate of the molten alloy, allowing longer times for gases to escape, thereby favoring a reduction in the porosity [104]. However, extended solidification times can also promote the coalescence of gas bubbles, which can eventually increase the pore size [105]. Furthermore, visual inspection of the build chamber revealed a color change in the powders spread on the platform at higher preheating temperatures, particularly at 500°C. One possible hypothesis could be that, despite the reduced oxygen content in the build chamber, some powder oxidation occurs, releasing gases during the melting step and thereby increasing porosity formation. Consequently, the non-linear trend observed for density and porosity across different preheating conditions should be the result of these competing mechanisms.

Another important observation from the results is that the cubes with the highest quality and those prematurely stopped during fabrication occupy very similar VED ranges. This outcome confirms the limitations of volumetric energy density in reliably predicting the final quality of L-PBF samples. Indeed, VED considers only a limited set of process parameters and cannot capture the complex phenomena governing the behavior of the melt pool [106]. Consequently, while VED can be useful for general predictions, it should not be used as the only criterion for quality assessment. More reliable quality predictions can be achieved by combining VED with in-process monitoring, which offers more detailed information on melt pool dynamics during fabrication [8]. This can also be complemented by theoretical indices — such as Fourier, Peclet, and Marangoni dimensionless numbers — that correlate material properties and process parameters with the melt pool behavior [31].

This consideration is further confirmed by the variation of the optimal VED range based on the three different preheating conditions. Specifically, at lower preheating temperatures, the optimal energy density is significantly higher, spanning between 80 and 105 J/mm^3, which aligns with other studies on Inconel 718 alloy reporting an optimal VED window of approximately 50 to 100 J/mm^3 [33], [44]. This behavior can be explained by the fact that platform preheating provides an additional energy input, which contributes to the melting process, but it is not taken into account in the standard VED formulation [107]. At a preheating temperature of 500°C, the optimal VED range was approximately similar to that of 300°C preheating, although slightly narrower. A plausible explanation for this behavior is that the used process parameters did not produce energy densities below that of the optimal range, leaving open the possibility that high-quality specimens could still be obtained at lower VEDs, consistent with the previous discussion.

To assess the eventual influence of build location on the quality of the printed component, a certain number of parameter combinations, for preheating temperatures of 80°C and 500°C, were duplicated. Thus, identical sets of process parameters were used to fabricate cubes in different regions of the platform. The analysis of the density revealed that, for parameters ensuring optimal density, the influence of the position was minimal. For instance, samples 80-S1 and 80-S4 and samples 500-S17 and 500-S20 exhibited comparable density values. However, when non-optimal parameters were considered, strong differences in density emerged. A striking example was observed for samples 80-S13 and 80-S16, which were produced with the same parameters but exhibited densities of 85% and 99%. These findings suggest that the build location can affect the overall quality of the samples, in particular under non-optimal process conditions. Explanations include spatter deposition in preferential regions depending on the direction of inert gas flow, which can additionally alter the spreading of the powders of subsequent layers [16].

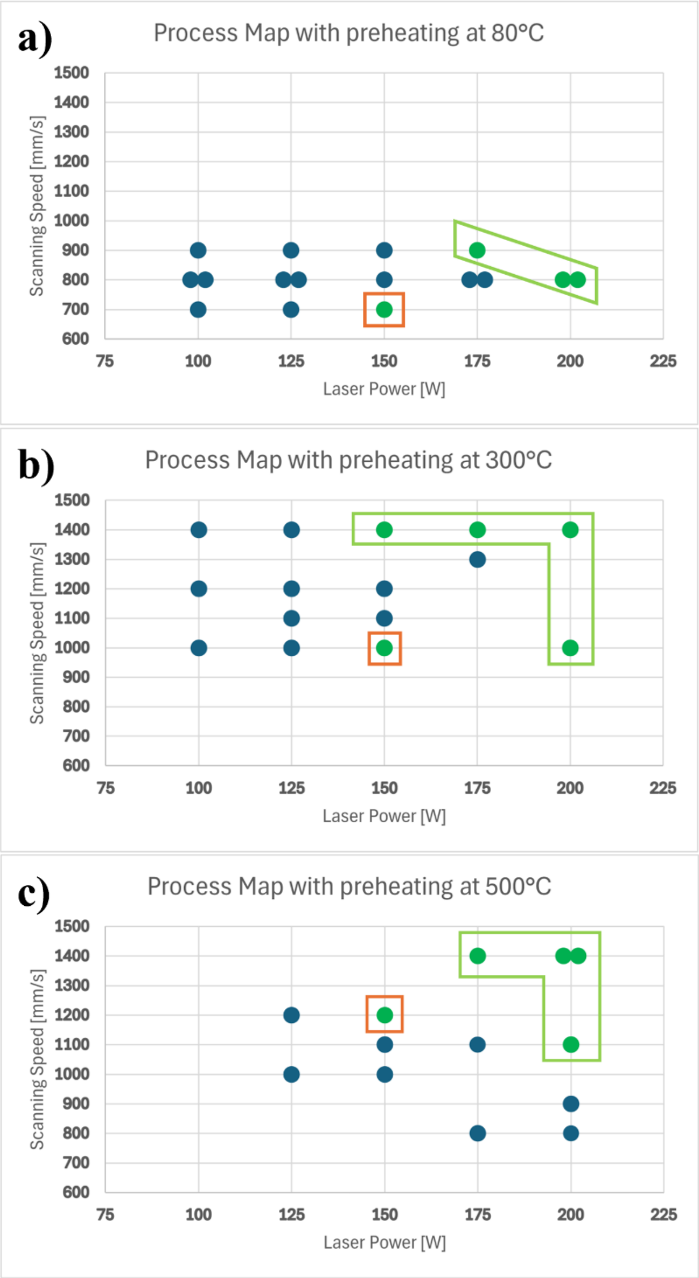

Figure 5.1 – Process maps for 80°C (a), 300°C (b), and 500°C (c) preheating temperatures. Samples highlighted in green boxes combine high measured density (>99.5 %) with defects not exceeding the critical size, whereas samples in orange boxes also exhibit high measured density but contain large defects

The process maps clearly show that, for each preheating condition considered, the optimal processing window always includes combinations of the highest laser powers and scanning speeds among the parameters investigated. Other samples exhibiting high measured density, highlighted by orange boxes in Figure 5.1, are located outside this optimal window; however, these specimens typically contain defects with dimensions exceeding the critical threshold, which could compromise the mechanical performance of the component.

5.2 Defect and Inclusion Evolution

In some of the highest-quality samples investigated through SEM, solidification cracks were detected. These defects are typically irregular in morphology, and their formation occurs during the final stages of the solidification process [14]. They originate when the solidifying layer contracts due to both solidification shrinkage and thermal contraction, while being constrained by the underlying substrate or previously deposited layers, which are typically at lower temperatures. This constraint causes the rise of tensile stresses within the solidifying layer; when these stresses exceed the strength of the metal, solidification cracks form [6], [108]. The inherently high cooling rates of the L-PBF process contribute to the intensification of thermal gradients within the material, thereby increasing the thermal stresses and promoting crack initiation [14].

Particularly, the occurrence of these defects was identified exclusively in the samples produced with a platform preheating of 80°C, corresponding to the lowest preheating condition. This observation suggests that increasing the preheating temperature reduces the likelihood of crack formation. This is consistent with findings reported in the literature, where preheating is described as one of the techniques used for crack mitigation [4], [6]. As previously discussed, preheating reduces the severe cooling rates typical of L-PBF technology, thereby lowering the thermal stresses generated within the material. In addition, it enhances the backfilling ability of the residual liquid metal, which has sufficient time to fill any cavities that may form during the final stages of solidification [105], [109].

Another critical microstructural feature identified in the analyzed specimens was the presence of oxide inclusions. These were generally non-spherical shaped and, due to their brittleness compared to the bulk alloy, can act as crack initiation sites, thereby reducing the overall strength and fatigue resistance of the material [6], [110].

Two distinct types of oxide inclusions were observed. The first type, with a needle-like morphology, exhibited EDX line profile peaks in Al and O, indicating the presence of Al_2O_3 particles. Such inclusions are commonly reported in Inconel 718 alloy produced by L-PBF, as other studies describe them, suggesting a great affinity of oxygen for aluminum, promoting the formation of alumina particles [111]. The second type consisted of segmented and irregularly shaped inclusions, with EDX profiles showing peaks in Si and O and a minor peak in Ti. While this chemical characterization suggests the presence of SiO_2 or more complex oxides containing possibly titanium. While no specific literature was found describing such inclusions in L-PBF Inconel 718, their morphology and composition indicate they may form through the segregation of Si and Ti during the solidification. These inclusions often aligned along grain boundaries, weakening them. Moreover, SiO_2 inclusions appeared distributed close to each other, forming sequences of particles that can act as crack initiation sites when subjected to applied stresses. The exclusive occurrence of cracks in samples fabricated with 80°C preheating could be explained by the combined effect of these inclusions and residual stresses. At higher preheating temperatures, reduced residual stresses may prevent these inclusions from initiating cracks, even if present.

In terms of size, the two types of inclusions exhibited distinct characteristics. The needle-like Al_2O_3 tended to be more compact, with dimensions up to 10 μm, whereas the segmented ones were generally smaller but often formed sequential arrangements extending to lengths up to 40 μm. Variations in platform preheating temperature did not significantly influence the occurrence or size of these inclusions; however, in samples fabricated at the highest preheating temperature, SiO_2 inclusions tended to coalesce, forming more compact structures.

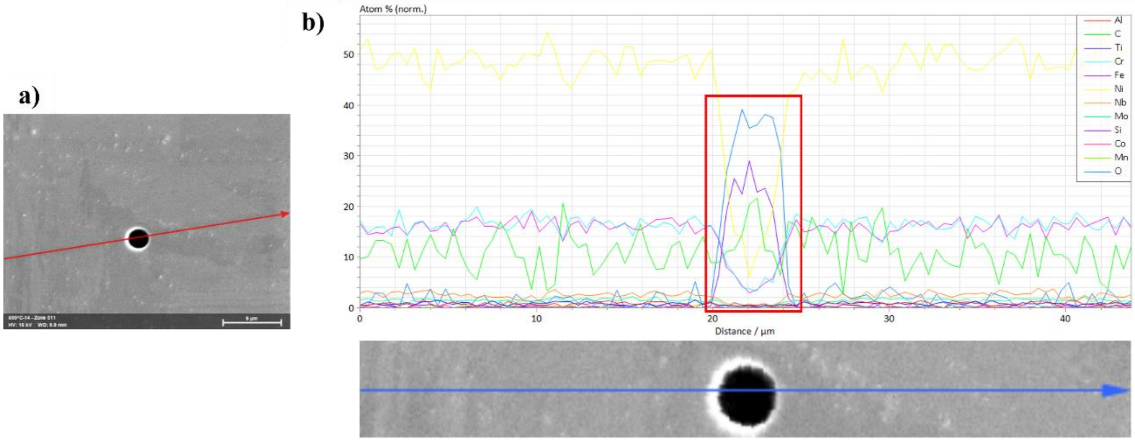

Figure 5.2 – SEM micrograph showing the coalescence of SiO_2 *inclusions in a sample fabricated with 500°C platform preheating (a) and the corresponding atomic percentage profile of the elements along the EDX line (b), with the red box highlighting Si and O peaks*

5.3 Influence of Process Parameters on Subgrain Boundaries and Size

The final polishing step, carried out with a colloidal silica suspension (OPS), allowed the removal of the surface strain-hardened layer, thereby enabling the SEM observation of the typical cellular substructure characteristic of alloys produced by L-PBF, without the necessity of etching. This morphology is generated as a consequence of the extreme cooling rates inherent to the process — typically in the range of 10^5 to 10^7 K/s — which induce constitutional supercooling ahead of the solidification front, leading to the development of this fine cellular structure [14], [33]. The visibility of these subgrains is enhanced by the different chemical composition between the cell boundaries, which are typically enriched in Nb, Mo, and Ti, and the Ni-rich γ-matrix [102].

The measured subgrain dimensions averaged approximately 0.4 microns, with maximum values reaching 1 µm, thus confirming their sub-micrometric extension, in agreement with previous studies on Inconel 718 alloy produced through L-PBF [33], [112]. Although the number of micrographs analyzed was insufficient to provide statistically robust data for a detailed comparison across different preheating conditions, a qualitative trend was observed: the dimensions of the subgrains appear to increase slightly with higher preheating temperatures. This behavior can be attributed to the reduction in cooling rate associated with higher preheating, which allows the coarsening of the subgrains [6].

The typical segregation of Nb at subgrain boundaries — widely reported in the literature and linked to the high cooling rates characteristics of the L-PBF process [33], [102], [113], [114] — was only slightly discernible in the EDX mapping, which instead revealed an overall chemical uniformity. This can be the consequence of a non-optimal spatial resolution for capturing such fine segregation. However, this does not imply that segregation is absent, but rather that it occurs at a scale below the detection capabilities of the used technique. Similar observations have been made by Bryndza et al. (2025), who reported Nb and Mo segregation in the as-built condition and identified it as a precursor to the formation of out-of-equilibrium detrimental phases, such as δ and Laves ones, along subgrain boundaries [115].

5.4 Impact of Parameters and Preheating on Hardness

The behavior of the hardness in the analyzed samples was evaluated through both macro-hardness and micro-hardness testing. Macro-hardness provided an average characterization of the bulk material, enabling a general comparison among different samples, while micro-hardness focused on localized measurements to capture potential microstructural changes.

Macro-hardness values range from 295 HV to 325 HV, coherently with typical ranges reported for L-PBF Inconel 718 in the as-built condition [18], [84], [116]. Micro-hardness measurements, instead, were generally higher and exhibited greater variability, ranging from 315 HV to 360 HV. This increase can be attributed to the indentation size effect, whereby smaller indentations tend to yield higher hardness values due to several factors [117].

When examining the effect of preheating temperature, macro-hardness results showed a decreasing trend: the average value dropped from 318 HV with 80°C platform preheating to around 305 HV for both 300°C and 500°C preheating. This reduction can be explained by the already mentioned slower cooling rates induced by higher preheating, which provides more time for grains and subgrains coarsening [14] Additionally, preheating facilitates stress relief by increasing atomic diffusion, allowing dislocation rearrangement [84]. Both phenomena contribute to the softening of the material, thus resulting in a reduced measured hardness.

For micro-hardness, the trend was initially similar, but the two samples produced with 500°C preheating displayed notable differences. One exhibited hardness values slightly higher than those of the 300°C specimens, while the other exceeded even the values of the 80°C specimens. This behavior suggests that preheating can trigger the precipitation of strengthening phases within the bulk alloy, thereby increasing the hardness [18], [84]. The magnitude of this effect likely depends on the different process parameters used, which can influence in a different way the extent of precipitation.

Regarding the type of precipitates, Chen et al. (2023) found an improvement of material strength due to MC carbide precipitation when increasing preheating temperature (from 200°C to 700°C) [108]. In addition, in the review published by Bryndza et al. (2025), heat accumulation during AM processing was reported to lead to in-situ aging with possible co-precipitation of γ' and γ'' structural intermetallic compounds that enhance strength [115]. Therefore, the precipitates responsible for the maximum micro-hardness achieved under preheating of 500°C can be intermetallic compounds, carbides, or both simultaneously. In all cases, the precipitation hardening achieved at 500°C preheating may be due to nanometric phases that are not detected by SEM observation. Overall, these results indicate that increasing preheating activates two competing mechanisms, which act in opposite ways to determine the final hardness of the material.

Chapter 6

CONCLUSIONS

After having studied the processing of L-PBF Inconel 718 alloy and checked for the influence of preheating temperature on internal soundness and microstructure of printed specimens in the as-built conditions, the following conclusions can be drawn:

- The VED ranges related to specimens with optimal quality (measured density greater than 99.5 %) overlapped with those of specimens that experienced premature interruption during the fabrication process. This overlap confirms the limitations of volumetric energy density in predicting the final quality. More accurate predictions require integrating VED and its correlated process parameters with additional tools, such as in-process monitoring and theoretical indices that take into consideration a broader range of influencing factors.
- A non-linear relationship between density and preheating temperature was observed, reflecting the activation of competing mechanisms, such as gas escaping and gas coalescence. Increasing platform preheating from 80°C to 300°C expanded the number of parameter combinations yielding densities greater than 99.5 %. In contrast, at 500°C preheating, porosity size increased, likely due to oxidation-related gas formation, limiting the maximum achievable density to values below 99.9 %, even for the best parameter combinations.
- Two distinct types of oxide inclusions were identified in the samples: needle-like Al_2O_3 particles, typical of L-PBF Inconel 718 alloy, and segmented SiO_2 inclusions, occasionally containing Ti and often located along grain boundaries. Both types likely originate from a combination of segregation occurring during the solidification and subsequent oxidation.
- Cracks were detected both in the presence and absence of Si-rich oxide inclusions, suggesting that they form due to limited backfilling during the solidification process and from the combination of residual stresses and

oxide inclusions, which act as initiation crack sites due to their morphology and distribution. Moreover, these cracks occurred exclusively in samples fabricated at the lowest preheating temperature, which was insufficient to effectively relieve thermal stresses.

- All the samples exhibited the fine cellular microstructure typical of L-PBF Inconel 718 alloy, with subgrain sizes averaging 0.4 µm. Qualitative observations suggested a slight coarsening of the subgrains with higher preheating temperatures, consistent with the effect of reduced cooling rates at higher temperatures.
- Macro-hardness values decreased with increasing preheating, most likely as a consequence of grain and subgrain coarsening and stress relief. Micro-hardness followed a similar trend; however, some specimens produced at 500°C displayed elevated values, suggesting localized precipitation of strengthening phases.

Chapter 7

PERSPECTIVES

The findings and criticalities identified in this work can be used as starting points for future research aimed at better understanding the observed phenomena. Some suggestions for the following studies can be:

- Further studies to assess how the positioning of samples on the build platform affects their final quality when fabricated under identical process parameters.
- Visual inspection during the preheating stage revealed color changes in the powder bed, leading to the hypothesis of possible oxidation occurring at higher preheating temperatures. A comparison between the chemical composition of original powders and those extracted from the powder bed after preheating could confirm whether oxidation has occurred.
- Adjusting VED formulation to include preheating temperature contribution and extended printing tests to help predict the modification of process maps location with preheating temperature evolution.
- Investigation of Si segregation occurrence, associated with Si-rich oxide inclusions, along grain boundaries, which leads to hot cracking when residual stresses are high enough (low preheating temperature). Further EBSD analyses on the samples exhibiting these features would enable precise mapping of their position relative to the grain structure.
- Consideration of more adapted techniques to better understand and identify the phases responsible for the precipitation hardening when increasing the preheating temperature.

Chapter 8

REFERENCES

[1] T. D. Ngo, A. Kashani, G. Imbalzano, K. T. Q. Nguyen, and D. Hui, “Additive manufacturing (3D printing): A review of materials, methods, applications and challenges,” *Compos. Part B Eng.*, vol. 143, pp. 172–196, June 2018, doi: 10.1016/j.compositesb.2018.02.012.

[2] S. Pramod and D. Kesavan, “Melting modes of laser powder bed fusion (L-PBF) processed IN718 alloy: Prediction and experimental analysis,” *Adv. Ind. Manuf. Eng.*, vol. 6, p. 100106, May 2023, doi: 10.1016/j.aime.2022.100106.

[3] A. Giorgetti, N. Baldi, M. Palladino, F. Ceccanti, G. Arcidiacono, and P. Citti, “A Method to Optimize Parameters Development in L-PBF Based on Single and Multitracks Analysis: A Case Study on Inconel 718 Alloy,” *Metals*, vol. 13, no. 2, p. 306, Feb. 2023, doi: 10.3390/met13020306.

[4] Q. Chen *et al.*, “Elucidating the effect of preheating temperature on melt pool morphology variation in Inconel 718 laser powder bed fusion via simulation and experiment,” *Addit. Manuf.*, vol. 37, p. 101642, Jan. 2021, doi: 10.1016/j.addma.2020.101642.

[5] T. Yue *et al.*, “Effects of volumetric energy density on melting modes, printability, microstructures, and mechanical properties of laser powder bed fusion (L-PBF) printed pure nickel,” *Mater. Sci. Eng. A*, vol. 909, p. 146871, Sept. 2024, doi: 10.1016/j.msea.2024.146871.

[6] T. DebRoy *et al.*, “Additive manufacturing of metallic components – Process, structure and properties,” *Prog. Mater. Sci.*, vol. 92, pp. 112–224, Mar. 2018, doi: 10.1016/j.pmatsci.2017.10.001.

[7] W. J. Sames, F. A. List, S. Pannala, R. R. Dehoff, and S. S. Babu, “The metallurgy and processing science of metal additive manufacturing,” *Int. Mater. Rev.*, vol. 61, no. 5, pp. 315–360, July 2016, doi: 10.1080/09506608.2015.1116649.

[8] R. K. Leach, D. Bourell, S. Carmignato, A. Donmez, N. Senin, and W. Dewulf, “Geometrical metrology for metal additive manufacturing,” *CIRP Ann.*, vol. 68, no. 2, pp. 677–700, Jan. 2019, doi: 10.1016/j.cirp.2019.05.004.

[9] N. Guo and M. C. Leu, “Additive manufacturing: technology, applications and research needs,” *Front. Mech. Eng.*, vol. 8, no. 3, pp. 215–243, Sept. 2013, doi: 10.1007/s11465-013-0248-8.

[10] D. Herzog, V. Seyda, E. Wycisk, and C. Emmelmann, “Additive manufacturing of metals,” *Acta Mater.*, vol. 117, pp. 371–392, Sept. 2016, doi: 10.1016/j.actamat.2016.07.019.

[11] A. Jiménez, P. Bidare, H. Hassanin, F. Tarlochan, S. Dimov, and K. Essa, “Powder-based laser hybrid additive manufacturing of metals: a review,” *Int. J. Adv. Manuf. Technol.*, vol. 114, no. 1–2, pp. 63–96, May 2021, doi: 10.1007/s00170-021-06855-4.

[12] L. Dowling, J. Kennedy, S. O'Shaughnessy, and D. Trimble, "A review of critical repeatability and reproducibility issues in powder bed fusion," *Mater. Des.*, vol. 186, p. 108346, Jan. 2020, doi: 10.1016/j.matdes.2019.108346.

[13] F42 Committee, *Terminology for Additive Manufacturing - General Principles - Terminology*. doi: 10.1520/F3177-21.

[14] S. Chowdhury *et al.*, "Laser powder bed fusion: a state-of-the-art review of the technology, materials, properties & defects, and numerical modelling," *J. Mater. Res. Technol.*, vol. 20, pp. 2109–2172, 2022, doi: 10.1016/j.jmrt.2022.07.121.

[15] S. R. Narasimharaju *et al.*, "A comprehensive review on laser powder bed fusion of steels: Processing, microstructure, defects and control methods, mechanical properties, current challenges and future trends," *J. Manuf. Process.*, vol. 75, pp. 375–414, Mar. 2022, doi: 10.1016/j.jmapro.2021.12.033.

[16] P. Bidare, I. Bitharas, R. M. Ward, M. M. Attallah, and A. J. Moore, "Fluid and particle dynamics in laser powder bed fusion," *Acta Mater.*, vol. 142, pp. 107–120, 2018, doi: 10.1016/j.actamat.2017.09.051.

[17] W. E. Frazier, "Metal Additive Manufacturing: A Review," *J. Mater. Eng. Perform.*, vol. 23, no. 6, pp. 1917–1928, June 2014, doi: 10.1007/s11665-014-0958-z.

[18] S. Sanchez *et al.*, "Powder Bed Fusion of nickel-based superalloys: A review," *Int. J. Mach. Tools Manuf.*, vol. 165, 2021, doi: 10.1016/j.ijmachtools.2021.103729.

[19] S. L. Sing and W. Y. Yeong, "Laser powder bed fusion for metal additive manufacturing: perspectives on recent developments," *Virtual Phys. Prototyp.*, vol. 15, no. 3, pp. 359–370, July 2020, doi: 10.1080/17452759.2020.1779999.

[20] J. Wang, R. Zhu, Y. Liu, and L. Zhang, "Understanding melt pool characteristics in laser powder bed fusion: An overview of single- and multi-track melt pools for process optimization," *Adv. Powder Mater.*, vol. 2, no. 4, p. 100137, Oct. 2023, doi: 10.1016/j.apmate.2023.100137.

[21] I. Gibson, D. Rosen, B. Stucker, and M. Khorasani, "Powder Bed Fusion," in *Additive Manufacturing Technologies*, I. Gibson, D. Rosen, B. Stucker, and M. Khorasani, Eds., Cham: Springer International Publishing, 2021, pp. 125–170. doi: 10.1007/978-3-030-56127-7_5.

[22] A. Mostafaei *et al.*, "Defects and anomalies in powder bed fusion metal additive manufacturing," *Curr. Opin. Solid State Mater. Sci.*, vol. 26, no. 2, p. 100974, Apr. 2022, doi: 10.1016/j.cossms.2021.100974.

[23] J. Mazumder, "1 - Laser-aided direct metal deposition of metals and alloys," in *Laser Additive Manufacturing*, M. Brandt, Ed., in Woodhead Publishing Series in Electronic and Optical Materials. , Woodhead Publishing, 2017, pp. 21–53. doi: 10.1016/B978-0-08-100433-3.00001-4.

[24] B. Lane *et al.*, "Transient Laser Energy Absorption, Co-axial Melt Pool Monitoring, and Relationship to Melt Pool Morphology," *Addit. Manuf.*, vol. 36, p. 10.1016/j.addma.2020.101504, Dec. 2020, doi: 10.1016/j.addma.2020.101504.

[25] J. Katagiri, S. Nomoto, M. Kusano, and M. Watanabe, "Particle Size Effect on Powder Packing Properties and Molten Pool Dimensions in Laser Powder Bed Fusion Simulation," *J. Manuf. Mater. Process.*, vol. 8, no. 2, p. 71, Apr. 2024, doi: 10.3390/jmmp8020071.

[26] M. S. Khandpur, A. Giubilini, L. Iuliano, and P. Minetola, "On the Use of Green and Blue Laser Sources for Powder Bed Fusion: State of the Art Review for Additive Manufacturing of Copper and Its Alloys," *Metals*, vol. 14, no. 12, p. 1464, Dec. 2024, doi: 10.3390/met14121464.

[27] O. Pannitz, F. Großwendt, A. Lüddecke, A. Kwade, A. Röttger, and J. T. Sehrt, "Improved Process Efficiency in Laser-Based Powder Bed Fusion of Nanoparticle Coated Maraging Tool Steel Powder," *Materials*, vol. 14, no. 13, p. 3465, June 2021, doi: 10.3390/ma14133465.

[28] L. E. T. Mathias *et al.*, "Metal powder as feedstock for laser-based additive manufacturing: From production to powder modification," *J. Mater. Res.*, vol. 39, no. 1, pp. 19–47, Jan. 2024, doi: 10.1557/s43578-023-01271-8.

[29] A. C. Field, L. N. Carter, N. J. E. Adkins, M. M. Attallah, M. J. Gorley, and M. Strangwood, "The Effect of Powder Characteristics on Build Quality of High-Purity Tungsten Produced via Laser Powder Bed Fusion (LPBF)," *Metall. Mater. Trans. A*, vol. 51, no. 3, pp. 1367–1378, Mar. 2020, doi: 10.1007/s11661-019-05601-6.

[30] W. Yuan *et al.*, "Oscillatory nature in melt-gas-powder interactions during laser powder bed fusion process revealed by CFD-DEM coupled modelling," *Virtual Phys. Prototyp.*, vol. 20, no. 1, p. e2446619, Dec. 2025, doi: 10.1080/17452759.2024.2446619.

[31] A. K. Agrawal, B. Rankouhi, and D. J. Thoma, "Predictive process mapping for laser powder bed fusion: A review of existing analytical solutions," *Curr. Opin. Solid State Mater. Sci.*, vol. 26, no. 6, p. 101024, Dec. 2022, doi: 10.1016/j.cossms.2022.101024.

[32] L. Zhang, Y. Li, Q. Zhang, and S. Zhang, "Microstructure evolution, phase transformation and mechanical properties of IN738 superalloy fabricated by selective laser melting under different heat treatments," *Mater. Sci. Eng. A*, vol. 844, p. 142947, June 2022, doi: 10.1016/j.msea.2022.142947.

[33] T. Huynh *et al.*, "Microstructural Development in Inconel 718 Nickel-Based Superalloy Additively Manufactured by Laser Powder Bed Fusion," *Metallogr. Microstruct. Anal.*, vol. 11, no. 1, pp. 88–107, Feb. 2022, doi: 10.1007/s13632-021-00811-0.

[34] N. Ren *et al.*, "Solute trapping and non-equilibrium microstructure during rapid solidification of additive manufacturing," *Nat. Commun.*, vol. 14, no. 1, p. 7990, Dec. 2023, doi: 10.1038/s41467-023-43563-x.

[35] J. P. Oliveira, A. D. LaLonde, and J. Ma, "Processing parameters in laser powder bed fusion metal additive manufacturing," *Mater. Des.*, vol. 193, p. 108762, Aug. 2020, doi: 10.1016/j.matdes.2020.108762.

[36] N. C. Levkulich, S. L. Semiatin, J. E. Gockel, J. R. Middendorf, A. T. DeWald, and N. W. Klingbeil, "The effect of process parameters on residual stress evolution and distortion in the laser powder bed fusion of Ti-6Al-4V," *Addit. Manuf.*, vol. 28, pp. 475–484, Aug. 2019, doi: 10.1016/j.addma.2019.05.015.

[37] N. Ahmed, I. Barsoum, G. Haidemenopoulos, and R. K. A. Al-Rub, "Process parameter selection and optimization of laser powder bed fusion for 316L stainless steel: A review," *J. Manuf. Process.*, vol. 75, pp. 415–434, Mar. 2022, doi: 10.1016/j.jmapro.2021.12.064.

[38] E. M. Sefene, "State-of-the-art of selective laser melting process: A comprehensive review," *J. Manuf. Syst.*, vol. 63, pp. 250–274, 2022, doi: 10.1016/j.jmsy.2022.04.002.

[39] K. G. Prashanth, S. Scudino, T. Maity, J. Das, and J. Eckert, "Is the energy density a reliable parameter for materials synthesis by selective laser melting?," *Mater.*

Res. Lett., vol. 5, no. 6, pp. 386–390, Nov. 2017, doi: 10.1080/21663831.2017.1299808.

[40] A. K. Agrawal, G. Meric De Bellefon, and D. Thoma, "High-throughput experimentation for microstructural design in additively manufactured 316L stainless steel," *Mater. Sci. Eng. A*, vol. 793, p. 139841, Aug. 2020, doi: 10.1016/j.msea.2020.139841.

[41] G. M. Volpato, U. Tetzlaff, and M. C. Fredel, "A comprehensive literature review on laser powder bed fusion of Inconel superalloys," *Addit. Manuf.*, vol. 55, 2022, doi: 10.1016/j.addma.2022.102871.

[42] U. Scipioni Bertoli, A. J. Wolfer, M. J. Matthews, J.-P. R. Delplanque, and J. M. Schoenung, "On the limitations of Volumetric Energy Density as a design parameter for Selective Laser Melting," *Mater. Des.*, vol. 113, pp. 331–340, Jan. 2017, doi: 10.1016/j.matdes.2016.10.037.

[43] M. A. Buhairi *et al.*, "Review on volumetric energy density: influence on morphology and mechanical properties of Ti6Al4V manufactured via laser powder bed fusion," *Prog. Addit. Manuf.*, vol. 8, no. 2, pp. 265–283, Apr. 2023, doi: 10.1007/s40964-022-00328-0.

[44] F. Caiazzo, V. Alfieri, and G. Casalino, "On the Relevance of volumetric energy density in the investigation of inconel 718 laser powder bed fusion," *Materials*, vol. 13, no. 3, 2020, doi: 10.3390/ma13030538.

[45] S. Sun, M. Brandt, and M. Easton, "2 - Powder bed fusion processes: An overview," in *Laser Additive Manufacturing*, M. Brandt, Ed., in Woodhead Publishing Series in Electronic and Optical Materials. , Woodhead Publishing, 2017, pp. 55–77. doi: 10.1016/B978-0-08-100433-3.00002-6.

[46] T. Mukherjee *et al.*, "Control of grain structure, phases, and defects in additive manufacturing of high-performance metallic components," *Prog. Mater. Sci.*, vol. 138, 2023, doi: 10.1016/j.pmatsci.2023.101153.

[47] S. Kramer, H. Wexel, A. Purwitasari, M. Jarwitz, V. Schulze, and F. Zanger, "Impact of different pore types on the tensile and fatigue properties of AlSi10Mg parts produced by laser powder bed fusion," *Prog. Addit. Manuf.*, Aug. 2025, doi: 10.1007/s40964-025-01288-x.

[48] P. Karimi, T. Raza, J. Andersson, and L.-E. Svensson, "Influence of laser exposure time and point distance on 75-μm-thick layer of selective laser melted Alloy 718," *Int. J. Adv. Manuf. Technol.*, vol. 94, no. 5, pp. 2199–2207, Feb. 2018, doi: 10.1007/s00170-017-1019-1.

[49] W. E. King *et al.*, "Observation of keyhole-mode laser melting in laser powder-bed fusion additive manufacturing," *J. Mater. Process. Technol.*, vol. 214, no. 12, pp. 2915–2925, Dec. 2014, doi: 10.1016/j.jmatprotec.2014.06.005.

[50] R. Li, J. Liu, Y. Shi, L. Wang, and W. Jiang, "Balling behavior of stainless steel and nickel powder during selective laser melting process," *Int. J. Adv. Manuf. Technol.*, vol. 59, no. 9–12, pp. 1025–1035, Apr. 2012, doi: 10.1007/s00170-011-3566-1.

[51] J. V. Gordon *et al.*, "Defect structure process maps for laser powder bed fusion additive manufacturing," *Addit. Manuf.*, vol. 36, p. 101552, Dec. 2020, doi: 10.1016/j.addma.2020.101552.

[52] B. Geddes, H. Leon, and X. Huang, *Superalloys - Alloying and Performance*. Materials Park, OH, United States: ASM International, 2010.

[53] J. B. Singh, “Introduction,” in *Alloy 625*, in Materials Horizons: From Nature to Nanomaterials. , Singapore: Springer Nature Singapore, 2022, pp. 1–27. doi: 10.1007/978-981-19-1562-8_1.

[54] H. Long, S. Mao, Y. Liu, Z. Zhang, and X. Han, “Microstructural and compositional design of Ni-based single crystalline superalloys — A review,” *J. Alloys Compd.*, vol. 743, pp. 203–220, Apr. 2018, doi: 10.1016/j.jallcom.2018.01.224.

[55] R. C. Reed, *The Superalloys: Fundamentals and Applications*, 1st ed. Cambridge University Press, 2006. doi: 10.1017/CBO9780511541285.

[56] A. Cladera, B. Weber, C. Leinenbach, C. Czaderski, M. Shahverdi, and M. Motavalli, “Iron-based shape memory alloys for civil engineering structures: An overview,” *Constr. Build. Mater.*, vol. 63, pp. 281–293, July 2014, doi: 10.1016/j.conbuildmat.2014.04.032.

[57] R. J. Kashinga, C. Mulubika, H. Mupeta, and B. Siyingwa, “An overview of the microstructure and mechanical behaviour of nickel-based superalloys,” *Acta Microsc.*, vol. 31, no. 2, Art. no. 2, Sept. 2022.

[58] A. P. Mouritz, Ed., “12 - Superalloys for gas turbine engines,” in *Introduction to Aerospace Materials*, Woodhead Publishing, 2012, pp. 251–267. doi: 10.1533/9780857095152.251.

[59] M. J. Donachie and S. J. Donachie, *Superalloys: a technical guide*, 2nd ed. Materials Park, Ohio London: ASM Blackwell, 2002.

[60] S. Bose, “Chapter 3 - SUBSTRATE ALLOYS,” in *High Temperature Coatings*, S. Bose, Ed., Burlington: Butterworth-Heinemann, 2007, pp. 17–27. doi: 10.1016/B978-075068252-7/50004-4.

[61] S. Mazumder, J. Boban, and A. Ahmed, “A Comprehensive Review of Recent Advancements in 3D-Printed Co-Cr-Based Alloys and Their Applications,” *J. Manuf. Mater. Process.*, vol. 9, no. 5, p. 169, May 2025, doi: 10.3390/jmmp9050169.

[62] J. Sato, T. Omori, K. Oikawa, I. Ohnuma, R. Kainuma, and K. Ishida, “Cobalt-Base High-Temperature Alloys,” *Science*, vol. 312, no. 5770, pp. 90–91, Apr. 2006, doi: 10.1126/science.1121738.

[63] M. Jovanović, “Nickel, cobalt and titanium-based alloys – from aircraft vehicles to medical applications - REVIEW,” *Metall. Mater. Eng.*, vol. 22, no. 3, pp. 205–220, Oct. 2016, doi: 10.30544/235.

[64] D. Coutsouradis, A. Davin, and M. Lamberigts, “Cobalt-based superalloys for applications in gas turbines,” *Mater. Sci. Eng.*, vol. 88, pp. 11–19, Apr. 1987, doi: 10.1016/0025-5416(87)90061-9.

[65] C. Sommitsch, R. Radis, A. Krumphals, M. Stockinger, and D. Huber, “Microstructure control in processing nickel, titanium and other special alloys,” in *Microstructure Evolution in Metal Forming Processes*, Elsevier, 2012, pp. 337–383. doi: 10.1533/9780857096340.3.337.

[66] T. M. Pollock and S. Tin, “Nickel-Based Superalloys for Advanced Turbine Engines: Chemistry, Microstructure and Properties,” *J. Propuls. Power*, vol. 22, no. 2, pp. 361–374, Mar. 2006, doi: 10.2514/1.18239.

[67] L. Liu, J. Zhang, and C. Ai, “Nickel-Based Superalloys,” in *Encyclopedia of Materials: Metals and Alloys*, F. G. Caballero, Ed., Oxford: Elsevier, 2022, pp. 294–304. doi: 10.1016/B978-0-12-803581-8.12093-4.

[68] S. Liu, S. McDonald, K. Sweatman, and K. Nogita, “The effects of precipitation strengthening and solid solution strengthening on strain rate sensitivity of lead-free solders: Review,” *Microelectron. Reliab.*, vol. 84, pp. 170–180, May 2018, doi: 10.1016/j.microrel.2018.03.038.

[69] A. J. Goodfellow, “Strengthening mechanisms in polycrystalline nickel-based superalloys,” *Mater. Sci. Technol.*, vol. 34, no. 15, pp. 1793–1808, Oct. 2018, doi: 10.1080/02670836.2018.1461594.

[70] M. A. Shaikh, M. Ahmad, K. A. Shoaib, J. I. Akhter, and M. Iqbal, “Precipitation hardening in Inconel* 625,” *Mater. Sci. Technol.*, vol. 16, no. 2, pp. 129–132, Feb. 2000, doi: 10.1179/026708300101507613.

[71] D. Deng, *Additively Manufactured Inconel 718 : Microstructures and Mechanical Properties*, vol. 1798. in Linköping Studies in Science and Technology. Licentiate Thesis, vol. 1798. Linköping: Linköping University Electronic Press, 2018. doi: 10.3384/lic.diva-144491.

[72] G. Lvov, V. I. Levit, and M. J. Kaufman, “Mechanism of primary MC carbide decomposition in Ni-base superalloys,” *Metall. Mater. Trans. A*, vol. 35, no. 6, pp. 1669–1679, June 2004, doi: 10.1007/s11661-004-0076-x.

[73] J. B. Singh, “Phases in Alloy 625,” in *Alloy 625*, in Materials Horizons: From Nature to Nanomaterials. , Singapore: Springer Nature Singapore, 2022, pp. 29–65. doi: 10.1007/978-981-19-1562-8_2.

[74] W. Xie, X. Yang, H. Yang, and X. Duan, “The effects of TiC particle on microstructure and mechanical properties of Inconel 718 fabricated by selective arc melting,” *J. Manuf. Process.*, vol. 131, pp. 1132–1142, Dec. 2024, doi: 10.1016/j.jmapro.2024.09.050.

[75] C. Y. Yap *et al.*, “Review of selective laser melting: Materials and applications,” *Appl. Phys. Rev.*, vol. 2, no. 4, p. 041101, Dec. 2015, doi: 10.1063/1.4935926.

[76] S. Abhishek, S. Anand Kumar, and S. Rao, “Multi-scale modelling for optimization of process parameters of laser powder bed fusion processed Inconel 718 surrogate part,” *Eng. Fail. Anal.*, vol. 155, p. 107713, Jan. 2024, doi: 10.1016/j.engfailanal.2023.107713.

[77] S. Singh and J. Andersson, “Heat-Affected-Zone Liquation Cracking in Welded Cast Haynes® 282®,” *Metals*, vol. 10, no. 1, p. 29, Jan. 2020, doi: 10.3390/met10010029.

[78] R. E. Schafrik, D. D. Ward, and J. R. Groh, “Application of Alloy 718 in GE Aircraft Engines: Past, Present and Next Five Years,” in *Superalloys 718, 625, 706 and Various Derivatives (2001)*, TMS, 2001, pp. 1–11. doi: 10.7449/2001/Superalloys_2001_1_11.

[79] J. Kolts, “Alloy 718 for the oil and gas industry,” *Superalloy*, vol. 718, pp. 329–344, 1989.

[80] N. Jeyaprakash, C.-H. Yang, and K. R. Ramkumar, “Microstructural, mechanical and wear behaviour of Inconel-718 produced through laser-powder bed-fused additive manufacturing,” *Mater. Sci. Technol.*, vol. 37, no. 3, pp. 326–337, Feb. 2021, doi: 10.1080/02670836.2021.1893457.

[81] T. G. Gallmeyer, S. Moorthy, B. B. Kappes, M. J. Mills, B. Amin-Ahmadi, and A. P. Stebner, “Knowledge of process-structure-property relationships to engineer better heat treatments for laser powder bed fusion additive manufactured Inconel 718,” *Addit. Manuf.*, vol. 31, p. 100977, Jan. 2020, doi: 10.1016/j.addma.2019.100977.

[82] W. M. Tucho and V. Hansen, “Characterization of SLM-fabricated Inconel 718 after solid solution and precipitation hardening heat treatments,” *J. Mater. Sci.*, vol. 54, no. 1, pp. 823–839, Jan. 2019, doi: 10.1007/s10853-018-2851-x.

[83] S. Mahadevan, S. Nalawade, J. B. Singh, A. Verma, B. Paul, and K. Ramaswamy, “Evolution of δ Phase Microstructure in Alloy 718,” in *Superalloy 718 and Derivatives*, 1st ed., E. A. Ott, J. R. Groh, A. Banik, I. Dempster, T. P. Gabb, R. Helmink, X. Liu, A. Mitchell, G. P. Sjöberg, and A. Wusatowska-Sarnek, Eds., Wiley, 2010, pp. 737–750. doi: 10.1002/9781118495223.ch57.

[84] W. M. Tucho, P. Cuvillier, A. Sjolyst-Kverneland, and V. Hansen, “Microstructure and hardness studies of Inconel 718 manufactured by selective laser melting before and after solution heat treatment,” *Mater. Sci. Eng. A*, vol. 689, pp. 220–232, Mar. 2017, doi: 10.1016/j.msea.2017.02.062.

[85] O. M. D. M. Messé, R. Muñoz-Moreno, T. Illston, S. Baker, and H. J. Stone, “Metastable carbides and their impact on recrystallisation in IN738LC processed by selective laser melting,” *Addit. Manuf.*, vol. 22, pp. 394–404, Aug. 2018, doi: 10.1016/j.addma.2018.05.030.

[86] A. Kreitcberg, V. Brailovski, and S. Turenne, “Elevated temperature mechanical behavior of IN625 alloy processed by laser powder-bed fusion,” *Mater. Sci. Eng. A*, vol. 700, pp. 540–553, July 2017, doi: 10.1016/j.msea.2017.06.045.

[87] F. Stein and A. Leineweber, “Laves phases: a review of their functional and structural applications and an improved fundamental understanding of stability and properties,” *J. Mater. Sci.*, vol. 56, no. 9, pp. 5321–5427, Mar. 2021, doi: 10.1007/s10853-020-05509-2.

[88] L. Huang, Y. Cao, G. Li, and Y. Wang, “Microstructure characteristics and mechanical behaviour of a selective laser melted Inconel 718 alloy,” *J. Mater. Res. Technol.*, vol. 9, no. 2, pp. 2440–2454, Mar. 2020, doi: 10.1016/j.jmrt.2019.12.075.

[89] Y.-L. Kuo, S. Horikawa, and K. Kakehi, “The effect of interdendritic δ phase on the mechanical properties of Alloy 718 built up by additive manufacturing,” *Mater. Des.*, vol. 116, pp. 411–418, Feb. 2017, doi: 10.1016/j.matdes.2016.12.026.

[90] A. Kurdi *et al.*, “Investigation into the Microstructure and Hardness of Additively Manufactured (3D-Printed) Inconel 718 Alloy,” *Materials*, vol. 16, no. 6, p. 2383, Mar. 2023, doi: 10.3390/ma16062383.

[91] N. Li, C. Wang, and C. Li, “Microstructures and High-Temperature Mechanical Properties of Inconel 718 Superalloy Fabricated via Laser Powder Bed Fusion,” *Materials*, vol. 17, no. 15, p. 3735, July 2024, doi: 10.3390/ma17153735.

[92] T.-T. Ikeshoji, Y. Tachibana, M. Yonehara, and H. Kyogoku, “Laser beam powder bed fusion of Inconel 718 under high power and scanning speed,” *J. Adv. Mech. Des. Syst. Manuf.*, vol. 17, no. 6, pp. JAMDSM0081–JAMDSM0081, 2023, doi: 10.1299/jamdsm.2023jamdsm0081.

[93] “Aconity3D GmbH - Additive Manufacturing,” Aconity3D. Accessed: Aug. 18, 2025. [Online]. Available: https://aconity3d.com/

[94] H. Jia, H. Sun, H. Wang, Y. Wu, and H. Wang, “Scanning strategy in selective laser melting (SLM): a review,” *Int. J. Adv. Manuf. Technol.*, vol. 113, no. 9, pp. 2413–2435, Apr. 2021, doi: 10.1007/s00170-021-06810-3.

[95] “CitoPress Apparecchiature per l’inglobamento | Struers.com.” Accessed: Aug. 18, 2025. [Online]. Available: https://www.struers.com/it-IT/Products/Mounting/Mounting-equipment/CitoPress#citopressfatti

[96] "Tegramin, macchina per la prelevigatura e lucidatura ad alta riproducibilità | Struers.com." Accessed: Aug. 18, 2025. [Online]. Available: https://www.struers.com/it-IT/Products/Grinding-and-Polishing/Grinding-and-polishing-equipment/Tegramin

[97] "Olympus BX60 BF/DF Transmitted and Reflected Light Microscope," Spectra Services. Accessed: Aug. 18, 2025. [Online]. Available: https://spectraservices.com/product/olympus-BX60F3-materials.html

[98] S.- https://www.smartly.cz and P. Skřivánek, "TESCAN CLARA | New Field-Free UHR SEM," TESCAN. Accessed: Aug. 18, 2025. [Online]. Available: https://www.tescan.com/tescan-clara-new-field-free-uhr-sem/

[99] "AccuPyc II 1345," Micromeritics. Accessed: Aug. 18, 2025. [Online]. Available: https://micromeritics.com/support/accupyc-ii-1345/

[100] "FALCON 500G2 | Automatic hardness tester," INNOVATEST. Accessed: Aug. 18, 2025. [Online]. Available: https://www.innovatest-europe.com/products/falcon-500g2/

[101] D. Bourell, J. Coholich, A. Chalancon, and A. Bhat, "Evaluation of energy density measures and validation for powder bed fusion of polyamide," *CIRP Ann.*, vol. 66, no. 1, pp. 217–220, Jan. 2017, doi: 10.1016/j.cirp.2017.04.128.

[102] G. V. de Leon Nope, L. I. Perez-Andrade, J. Corona-Castuera, D. G. Espinosa-Arbelaez, J. Muñoz-Saldaña, and J. M. Alvarado-Orozco, "Study of volumetric energy density limitations on the IN718 mesostructure and microstructure in laser powder bed fusion process," *J. Manuf. Process.*, vol. 64, pp. 1261–1272, Apr. 2021, doi: 10.1016/j.jmapro.2021.02.043.

[103] J.-S. L. Bernsmann, S. Hillebrandt, M. Rommerskirchen, S. Bold, and J. H. Schleifenbaum, "On the Use of Metal Sinter Powder in Laser Powder Bed Fusion Processing (PBF-LB/M)," *Materials*, vol. 16, no. 16, p. 5697, Aug. 2023, doi: 10.3390/ma16165697.

[104] S. Sinha and T. Mukherjee, "Mitigation of Gas Porosity in Additive Manufacturing Using Experimental Data Analysis and Mechanistic Modeling," *Materials*, vol. 17, no. 7, p. 1569, Mar. 2024, doi: 10.3390/ma17071569.

[105] K. Riener, T. Pfalz, F. Funcke, and G. Leichtfried, "Processability of high-strength aluminum 6182 series alloy via laser powder bed fusion (LPBF)," *Int. J. Adv. Manuf. Technol.*, vol. 119, no. 7, pp. 4963–4977, Apr. 2022, doi: 10.1007/s00170-022-08673-8.

[106] U. Scipioni Bertoli, A. J. Wolfer, M. J. Matthews, J.-P. R. Delplanque, and J. M. Schoenung, "On the limitations of Volumetric Energy Density as a design parameter for Selective Laser Melting," *Mater. Des.*, vol. 113, pp. 331–340, Jan. 2017, doi: 10.1016/j.matdes.2016.10.037.

[107] S. Qin, Y. Bo, S. Herzog, B. Hallstedt, A. Kaletsch, and C. Broeckmann, "Influence of Process Parameters on Porosity and Hot Cracking of AISI H13 Fabricated by Laser Powder Bed Fusion," *Powders*, vol. 1, no. 3, Art. no. 3, Sept. 2022, doi: 10.3390/powders1030012.

[108] Y. Chen *et al.*, "Effect of high preheating on the microstructure and mechanical properties of high gamma prime Ni-based superalloy manufactured by laser powder bed fusion," *J. Alloys Compd.*, vol. 960, p. 170598, Oct. 2023, doi: 10.1016/j.jallcom.2023.170598.

[109] M. Abdelwahed *et al.*, "Cracking mechanisms and effect of extensive preheating in CM247LC and IN713LC Ni-base superalloy processed by Laser Powder Bed

Fusion," *Mater. Today Commun.*, vol. 37, p. 107644, Dec. 2023, doi: 10.1016/j.mtcomm.2023.107644.

[110] T. Ohtsuki and P. C. Pistorius, "Oxide Behavior During Laser Surface Melting," *Metals*, vol. 15, no. 6, p. 627, May 2025, doi: 10.3390/met15060627.

[111] L. A. Smith and P. C. Pistorius, "Build Surface Roughness and Internal Oxide Concentration for Laser Powder Bed Fusion of IN718," *J. Manuf. Mater. Process.*, vol. 6, no. 1, p. 25, Feb. 2022, doi: 10.3390/jmmp6010025.

[112] M. E. Aydinöz *et al.*, "On the microstructural and mechanical properties of post-treated additively manufactured Inconel 718 superalloy under quasi-static and cyclic loading," *Mater. Sci. Eng. A*, vol. 669, pp. 246–258, July 2016, doi: 10.1016/j.msea.2016.05.089.

[113] L. Zhou, A. Mehta, B. McWilliams, K. Cho, and Y. Sohn, "Microstructure, precipitates and mechanical properties of powder bed fused inconel 718 before and after heat treatment," *J. Mater. Sci. Technol.*, vol. 35, no. 6, pp. 1153–1164, June 2019, doi: 10.1016/j.jmst.2018.12.006.

[114] Y. Wen *et al.*, "Laser powder bed fusion of compositionally graded CoCrMo-Inconel 718," *Addit. Manuf.*, vol. 40, p. 101926, Apr. 2021, doi: 10.1016/j.addma.2021.101926.

[115] G. Bryndza *et al.*, "Review of the Microstructural Impact on Creep Mechanisms and Performance for Laser Powder Bed Fusion Inconel 718," *Materials*, vol. 18, no. 2, p. 276, Jan. 2025, doi: 10.3390/ma18020276.

[116] B. Farhang *et al.*, "Investigating the Effect of Heat Transfer on the Homogenity in Microstructure and Properties of Inconel 718 Alloy Fabricated by Laser Powder Bed Fusion Technique," 2021, *University of Texas at Austin*. doi: 10.26153/TSW/17620.

[117] J. Petrík, P. Blaško, Š. Markulík, M. Šolc, and P. Palfy, "The Indentation Size Effect (ISE) of Metals," *Crystals*, vol. 12, no. 6, p. 795, June 2022, doi: 10.3390/cryst12060795.

Chapter 9

ANNEXES

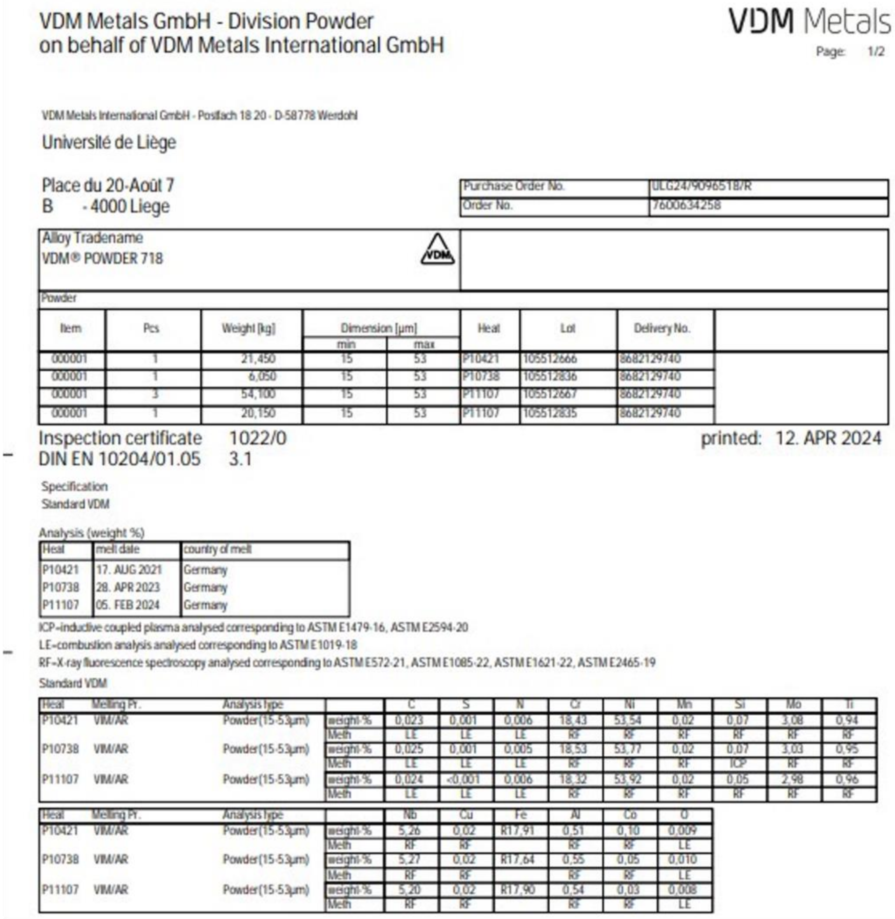

VDM Metals GmbH - Division Powder
on behalf of VDM Metals International GmbH

VDM Metals
Page: 1/2

VDM Metals International GmbH - Postfach 18 20 - D-58778 Werdohl

Université de Liège

Place du 20-Août 7
B - 4000 Liege

Purchase Order No.	ULG24/9096518/R
Order No.	7600634258

Alloy Tradename
VDM® POWDER 718

Powder

Item	Pcs	Weight [kg]	Dimension [µm]		Heat	Lot	Delivery No.
			min	max			
000001	1	21,450	15	53	P10421	105512666	8682129740
000001	1	6,050	15	53	P10738	105512836	8682129740
000001	3	54,100	15	53	P11107	105512667	8682129740
000001	1	20,150	15	53	P11107	105512835	8682129740

Inspection certificate 1022/0
DIN EN 10204/01.05 3.1

printed: 12. APR 2024

Specification
Standard VDM

Analysis (weight %)

Heat	melt date	country of melt
P10421	17. AUG 2021	Germany
P10738	28. APR 2023	Germany
P11107	05. FEB 2024	Germany

ICP=inductive coupled plasma analysed corresponding to ASTM E1479-16, ASTM E2594-20
LE=combustion analysis analysed corresponding to ASTM E1019-18
RF=X-ray fluorescence spectroscopy analysed corresponding to ASTM E572-21, ASTM E1085-22, ASTM E1621-22, ASTM E2465-19

Standard VDM

Heat	Melting Pr.	Analysis type		C	S	N	Cr	Ni	Mn	Si	Mo	Ti
P10421	VIM/AR	Powder(15-53µm)	weight-%	0,023	0,001	0,006	18,43	53,54	0,02	0,07	3,08	0,94
			Meth	LE	LE	LE	RF	RF	RF	RF	RF	RF
P10738	VIM/AR	Powder(15-53µm)	weight-%	0,025	0,001	0,005	18,53	53,77	0,02	0,07	3,03	0,95
			Meth	LE	LE	LE	RF	RF	RF	ICP	RF	RF
P11107	VIM/AR	Powder(15-53µm)	weight-%	0,024	<0,001	0,006	18,32	53,92	0,02	0,05	2,98	0,96
			Meth	LE	LE	LE	RF	RF	RF	RF	RF	RF

Heat	Melting Pr.	Analysis type		Nb	Cu	Fe	Al	Co	O
P10421	VIM/AR	Powder(15-53µm)	weight-%	5,26	0,02	R17,91	0,51	0,10	0,009
			Meth	RF	RF		RF	RF	LE
P10738	VIM/AR	Powder(15-53µm)	weight-%	5,27	0,02	R17,64	0,55	0,05	0,010
			Meth	RF	RF		RF	RF	LE
P11107	VIM/AR	Powder(15-53µm)	weight-%	5,20	0,02	R17,90	0,54	0,03	0,008
			Meth	RF	RF		RF	RF	LE

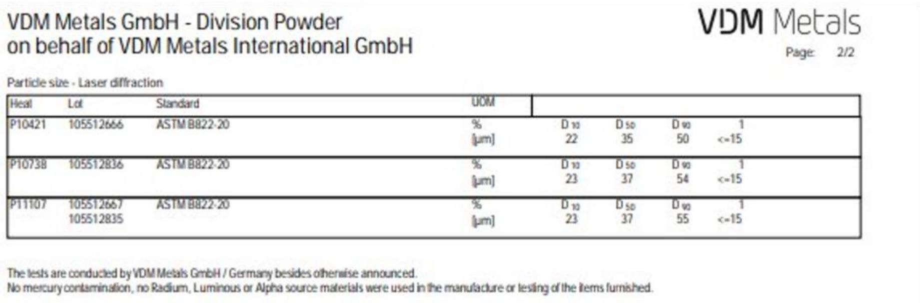

VDM Metals GmbH - Division Powder
on behalf of VDM Metals International GmbH

VDM Metals
Page: 2/2

Particle size - Laser diffraction

Heat	Lot	Standard	UOM				
P10421	105512666	ASTM B822-20	%	D_{10}	D_{50}	D_{90}	1
			[µm]	22	35	50	<=15
P10738	105512836	ASTM B822-20	%	D_{10}	D_{50}	D_{90}	1
			[µm]	23	37	54	<=15
P11107	105512667 105512835	ASTM B822-20	%	D_{10}	D_{50}	D_{90}	1
			[µm]	23	37	55	<=15

The tests are conducted by VDM Metals GmbH / Germany besides otherwise announced.
No mercury contamination, no Radium, Luminous or Alpha source materials were used in the manufacture or testing of the items furnished.